Applied Energy 426 (2026) 128623

Contents lists available at ScienceDirect

Applied Energy

journal homepage: www.elsevier.com/locate/apenergy

Evaluating isothermal degradation error in lithium-ion batteries under WLTP drive cycles

Nadim Ahmed, Md Fazle Hasan Shiblee, Theodore Azemtsop Manfo *

Department of Electrical Engineering and Energy Technology, School of Technology and Innovations, University of Vaasa, Wolffintie 34, Vaasa 65200, Finland

HIGHLIGHTS

- SEI activation energy governs isothermal ΔSOH error, not the drive-cycle thermal gradient.
- Two-stage activation-energy calibration reduces RMSE from 9.1 to 1.45 percentage points.
- Isothermal assumptions cause up to 8.2 percentage points of SOH error over 500 cycles.
- SEI dominates NMC capacity loss (>99%), while active-material loss reaches 38% in LFP cells.
- Uncertainty analysis confirms robustness across activation energies of 62–95 kJ mol^{-1}.

GRAPHICAL ABSTRACT

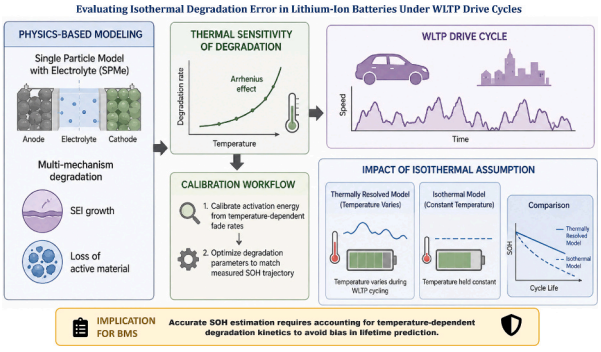

ARTICLE INFO

Keywords:
Lithium-ion battery degradation
Solid electrolyte interphase activation energy
Isothermal modelling error
Worldwide harmonised light vehicle test procedure
Battery management system

ABSTRACT

Physics-based battery management systems frequently assume isothermal cell oper-ation, eliminating the thermal sub-model to reduce computational cost. The error introduced by this assumption in state-of-health prediction depends on the activation energy of the solid electrolyte interphase kinetic rate constant. In widely used pa-rameterisations this energy is set to zero, decoupling temperature from degradation kinetics and concealing the true thermal sensitivity. A calibrated multi-mechanism Single Particle Model with Electrolyte is developed for nickel manganese cobalt oxide and lithium iron phosphate cells. A two-stage sequential procedure calibrates the ac-tivation energy from temperature-dependent fade rate ratios, then jointly optimises the solid electrolyte interphase rate constant and loss of active material coefficient against a longitudinal state-of-health trajectory, achieving a root mean square er-ror of 1.45 pp. — 6.3-fold improvement over the uncalibrated default. A parametric sweep of 24 conditions spanning both chemistries, ambient temperatures of 10, 25, and 40 °C, and charge rates of 1C and 2C shows that the isothermal assumption in-troduces state-of-health errors of 1.4–8.2 pp. (for nickel manganese cobalt oxide) over 500 Worldwide Harmonised Light Vehicle Test Procedure cycles with the calibrated activation energy of 78.5 kJ mol^{-1}, compared with a maximum of 0.20 pp. at zero ac-tivation energy. For nickel manganese cobalt oxide cells, solid electrolyte interphase growth accounts for >99% of capacity loss. For lithium iron phosphate cells, solid electrolyte interphase and loss of active material contribute approximately 62% and 38% respectively, due to the larger depth of discharge per cycle. A three-layer parameter uncertainty analysis one-at-a-time sensitivity, an activation energy sweep across 62–95 kJ mol^{-1}, and an

* Corresponding author.
E-mail addresses: x0181596@student.uwasa.fi (N. Ahmed), x3082155@student.uwasa.fi (M.F.H. Shiblee), theodore.azemtsop.manfo@uwasa.fi (T.A. Manfo).

https://doi.org/10.1016/j.apenergy.2026.128623
Received 10 June 2026; Received in revised form 14 July 2026; Accepted 2 August 2026
Available online 12 August 2026

analytical Monte Carlo, confirms that the isothermal ΔSOH error exceeds 0.5 pp. across the full physically plausible parameter space and that activation energy is the dominant source of uncertainty.

1. Introduction

Electric vehicle (EV) battery packs degrade irreversibly through every charge and discharge cycle, reducing the usable capacity and available power of the pack over its service life. The battery management system (BMS) must track this degradation in real time by estimating the sate of health (SOH), defined as the ratio of current discharge capacity to the nominal capacity at the beginning of life. Accurate SOH estimation enables correct range prediction, timely warranty assessments, and safe end-of-life decisions [1]. The global EV fleet exceeded 40 million vehicles in 2023, and accurate lifetime prediction is increasingly central to both vehicle operation and the emerging second life battery market [2]. SOH estimation methods range from electrochemical impedance spectroscopy [3] to machine learning [4] and physics based electrochemical models [5]. Battery chemistry advances, including next-generation olivine-based materials, are expanding the range of chemistries for which physics-based models must remain accurate [6]. The economic cost of SOH estimation errors is substantial: an overestimate accelerates undetected capacity fade and risks premature cell failure, while an underestimate triggers unnecessary pack replacement [7].

1.1. Electrochemical models for state-of-health estimation

Physics based electrochemical models are used in BMS algorithms because they generalize mechanistically to operating conditions outside the calibration dataset, unlike empirical or data-driven approaches that require representative training data covering the full operating space [8]. The Doyle–Fuller–Newman (DFN) model resolves concentration and potential fields across both electrodes and the separator [9], but its computational cost prohibits real time embedded deployment. The Single Particle Model (SPM) reduces each electrode to a single representative spherical particle, enabling analytical solutions in some regimes, but neglects electrolyte dynamics and loses accuracy above approximately 1C [10]. The Single Particle Model with Electrolyte (SPMe) through a systematic asymptotic reduction of the DFN equations, recovers electrolyte gradient effects through a leading order correction [11] and retains accuracy up to approximately 2C for standard graphite electrodes [12] through rigorous error bounds. Richardson et al. extend the SPMe validity analysis to graded electrodes, demonstrating conditions under which the asymptotic reduction remains accurate at elevated rates [13].

The SPMe therefore occupies a practically important position for BMS deployment: it is computationally tractable for embedded processors yet physically richer than the SPM. Recent BMS implementations based on the SPMe have demonstrated real time state estimation with update rates compatible with commercial BMS hardware [14]. Accurate thermal management is a prerequisite for these implementations; the heat rejection coefficient of the cell constrains the steady state temperature during continuous cycling [15], and inadequate thermal management leads to accelerated degradation [16].

1.2. Degradation mechanisms in lithium-ion cells

Capacity fade in lithium-ion cells arises from three principal electrochemical and mechanical processes. The solid electrolyte interphase (SEI) grows at the surface of the negative electrode through the continuous electrochemical reduction of electrolyte solvent, consuming cyclable lithium inventory and increasing cell impedance [1]. The chemical composition and growth kinetics of the SEI depend on the electrolyte formulation and electrode surface chemistry [17]. The electrode surface chemistry governing SEI kinetics varies with cathode material; olivine-phosphate systems such as $LiFePO_4$ exhibit distinct SEI formation characteristics compared with NMC [18,19]. The SEI mechanism is dominant under normal cycling conditions and follows Arrhenius kinetics, accelerating exponentially with temperature. Experimental studies have reported activation energy values in the range of 60–80 kJ mol^{-1} for graphite based cells, which governs the temperature dependence of the degradation process [20,21]. Calendar aging studies confirm the temperature dependence of SEI growth in both nickel manganese cobalt oxide (NMC) and lithium iron phosphate (LFP) chemistries [22].

Loss of active material (LAM) reduces the number of lithium storage sites through particle fracture, contact loss between electrode particles and the binder matrix, and transition metal dissolution from the cathode [8]. LAM is driven by mechanical stresses associated with volume changes during lithiation and delithiation [23]. Under standard driving duty cycles, where depth of discharge per trip rarely exceeds 20%, LAM accumulates slowly because the mechanical strain is limited. The stress driven LAM in graphite anodes accelerates substantially only under deep cycling, a condition not routinely present in the Worldwide Harmonised Light Vehicle Test Procedure (WLTP) operation [24]. Long term accelerated aging studies on NMC cells [25] confirm that LAM becomes significant only after approximately 300–500 full cycles under aggressive charge protocols. Structural studies of $LiMPO_4$-type cathodes confirm that transition metal dissolution is suppressed in phosphate frameworks, supporting the SEI-dominant degradation pathway assumed in this model [26,27].

Irreversible lithium plating occurs when the overpotential at the negative electrode surface falls below zero, depositing metallic lithium on the graphite surface rather than intercalating it into the lattice [28]. A fraction of plated lithium becomes electrically isolated dead lithium, causing permanent capacity loss. Further study developed a comprehensive plating model validated against multiple cell chemistries, establishing that plating risk peaks at sub zero ambient temperatures and charge rates above 2C [1]. Post mortem analyses of commercially cycled cells confirm the presence of plated lithium under cold climate fast charging conditions [29]. Electrolyte oxidation at the cathode surface at elevated voltages constitutes an additional degradation mechanism not included in the present model but documented in NMC cells [30]. Cathode-side degradation mechanisms and electrolyte oxidation pathways differ substantially across chemistries [31].

1.3. Temperature dependence and the isothermal assumption

BMS degradation models frequently adopt the isothermal assumption: the cell temperature is fixed at the ambient value and the thermal sub model is omitted [32]. The motivation is computational efficiency. The thermal state adds one ordinary differential equation to the model, which is small in absolute terms but eliminates a hardware requirement for cell temperature sensing in the core state estimator.

The isothermal assumption introduces a systematic error whenever internal heat generation shifts the cell temperature from the ambient value during cycling, because SEI growth rate depends on temperature through the Arrhenius relation. The magnitude of this error depends on two independent factors: the thermal gradient generated during the duty cycle and the activation energy E_a of the SEI kinetics. The first factor is determined by the duty cycle and cell thermal properties. The second factor is a cell material property that must be experimentally calibrated.

The critical problem identified in this study is that widely used parameterisations, including the Chen2020 parameter set [33], assign $E_a = 0$ to the SEI rate constant. This choice decouples temperature from degradation kinetics entirely: both the isothermal and thermally

coupled models predict identical SOH trajectories regardless of the thermal gradient. Prior computational studies that compare isothermal and thermally coupled models while using $E_a = 0$ will therefore always report a negligible thermal effect, not because the isothermal assumption is physically justified, but because the parameterisation prevents any thermal effect from manifesting. This confound has not been systematically identified or corrected in the existing literature.

1.4. The worldwide harmonised light vehicle test procedure as an operating scenario

The WLTP Class 3b is the regulatory standard for EV energy consumption and range certification in the European Union, Japan, India, South Korea, and Australia [34]. It defines a 1800-s speed time trace comprising four phases (Low, Medium, High, and Extra High) that represent urban, suburban, and motorway driving with frequent stops, accelerations, and regenerative braking events. The net depth of discharge per 30-min WLTP pass is typically 5–12% of cell capacity, depending on vehicle and pack specifications. This shallow, intermittent loading generates modest cell temperature gradients per cycle, making WLTP a representative and physically relevant scenario for studying whether the isothermal assumption is sufficient.

Previous studies demonstrated that WLTP equivalent cycling can reproduce degradation trends consistent with field observations, supporting the use of WLTP as a representative lifetime stress protocol [35]. It has also been shown that degradation pathways under realistic drive and grid operation differ substantially from those observed under constant current cycling, highlighting the importance of realistic duty cycle representation [36]. Nevertheless, these works employed empirical degradation correlations instead of physics based electrochemical degradation models and did not evaluate the effect of thermal coupling on prediction accuracy. As a result, the relationship between drive cycle realism and electrochemical model fidelity remains insufficiently explored.

1.5. Prior work on calibrated degradation models

Table 1 summarizes representative physics based degradation studies that are directly relevant to the present work. The comparison dimensions are: electrochemical model type, thermal model type, degradation mechanisms included, the activation energy treatment, and whether a drive cycle protocol was used for simulation.

SPM = single particle model; SPMe = single particle model with electrolyte; DFN = Doyle–Fuller–Newman model; CC = constant-current; LAM = loss of active material; SEI = solid electrolyte interphase.

Based on the literature review, three research gaps can be identified:

- Prior comparisons of isothermal and thermally coupled models have been conducted with $E_a = 0$, preventing any thermal effect from appearing in the results. The sensitivity of the isothermal ΔSOH error to the true activation energy value has not been studied systematically.
- Existing calibrations are performed against constant current accelerated aging data. The combination of intermittent loading, three ambient temperatures, two charge rates, and two chemistries has not been studied within a single consistent electrochemical thermal framework.
- Mechanism decomposition studies [8] have been conducted under constant current protocols. It is not established whether loss of active material and plating make significant contributions under the shallow, intermittent loading of a standard drive cycle.

This paper addresses all three gaps. The present study differs from prior work in three respects: activation energy is calibrated from multi-temperature fade rate data rather than assumed zero; the resulting isothermal ΔSOH error is quantified across 24 conditions spanning two chemistries, three temperatures, and two charge rates under a standard drive cycle; and a three-layer uncertainty analysis confirms that the finding is robust across the physically plausible parameter space. The

Table 1
Summary of representative physics-based battery degradation studies.

Study	EChem	Thermal	Mechanisms	Ea treatment	Key limitation
Safari et al. [37]	SPM	Isothermal	SEI	Not calibrated	Single chemistry; CC cycling only
Ecker et al. [25]	Empirical	Isothermal	SEI, LAM	Empirical fit	NMC only; no drive-cycle validation
Schimpe et al. [20]	Empirical	Lumped	SEI	Calibrated (62 kJ mol^{-1})	LFP only
Prada et al. [38]	SPMe	Lumped	SEI	Not calibrated	No activation-energy calibration
Naumann et al. [22]	Empirical	N/A	Calendar SEI	Not calibrated	Calendar aging only
Kabitz et al. [39]	Empirical	Isothermal	SEI, LAM	Empirical fit	No thermal coupling
Ai et al. [24]	SPMe	Thermo-mech.	SEI, mechanical	Ea = 0	Pouch-cell specific
Reniers et al. [8]	SPMe	Isothermal	SEI, LAM	Ea = 0	No thermal comparison
Timms et al. [12]	SPMe	Isothermal	None	N/A	Model-reduction study
Richardson et al. [13]	SPMe	Isothermal	None	N/A	Focus on graded electrodes
Marquis et al. [11]	SPMe	Isothermal	SEI	Ea = 0	CC operation only
Tosi et al. [35]	Empirical	N/A	Empirical	N/A	No electrochemical model
Dubarry et al. [36]	Empirical	N/A	Empirical	N/A	No physics-based model
O'Kane et al. [28]	SPMe	Isothermal	Plating	N/A	Plating mechanism only
O'Kane et al. [1]	SPMe	Isothermal	SEI, LAM, plating	Not calibrated	No drive-cycle validation
Sulzer et al. [40]	SPMe/DFN	Isothermal	SEI	Ea = 0	Software-oriented study
Rinkel et al. [41]	None	N/A	Cathode	N/A	Experimental only
Dose et al. [30]	None	N/A	SEI, cathode	N/A	Experimental only
Attia et al. [42]	Data-driven	N/A	Empirical	N/A	No mechanism-level interpretation
Severson et al. [43]	Data-driven	N/A	Empirical	N/A	No physics-based degradation
Jeon et al. [44]	Empirical	Isothermal	SEI, LAM	Not calibrated	Review only; no physics-based thermal comparison
Li et al. [45]	SPMe/DFN	Isothermal	SEI, LAM, plating	Calibrated	No drive-cycle; no isothermal vs. thermal comparison
Zhang et al. [46]	DFN	Isothermal	SEI, LAM, plating, cracking	$E_a = 0$	Synthetic data only; no thermal coupling
Wheeler et al. [47]	None	N/A	Empirical	N/A	Experimental; no physics-based model
This work	**SPMe**	**Lumped**	**SEI, LAM, plating**	**NMC calibrated; LFP from literature**	**Drive-cycle validation, multi-chemistry**

main contributions are as follows:

- A two-stage sequential calibration procedure is introduced that calibrates the solid electrolyte interphase activation energy from temperature-dependent fade rate ratios before optimizing the absolute rate constants. This procedure avoids the degenerate single-parameter minimum that invalidated prior calibration attempts with zero activation energy, and establishes the calibrated value $E_a = 78.5$ kJ mol^{-1}.
- A controlled comparison between an isothermal model and a lumped thermal model over 500 Worldwide Harmonised Light Vehicle Test Procedure drive cycles is reported for both the default parameterisation ($E_a = 0$) and the calibrated parameterisation ($E_a = 78.5$ kJ mol^{-1}), establishing that the isothermal ΔSOH error is 0.20 pp. under the default and 1.4–8.2 pp. (for NMC) under the calibrated parameterisation.
- A 24-condition parametric sweep spanning nickel manganese cobalt oxide and lithium iron phosphate chemistries, three ambient temperatures (-10, 25, 40 °C), and two charge rates (1C, 2C) is conducted using the calibrated multi-mechanism SPMe, providing the first systematic quantification of isothermal model error under drive cycle conditions across multiple chemistries.
- Mechanism-resolved capacity loss analysis shows that, for NMC, solid electrolyte interphase growth accounts for >99% of total capacity loss, with loss of active material and plating each below 0.015% of nominal capacity. For LFP at 1C, solid electrolyte interphase contributes approximately 62% and loss of active material approximately 38% of total capacity loss, reflecting LFP's larger depth of discharge per Worldwide Harmonised Light Vehicle Test Procedure cycle. The conditions under which plating becomes non-negligible are identified.
- A three-layer parameter uncertainty analysis comprising one-at-a-time local sensitivity perturbation, a deterministic activation energy sweep across 62–95 kJ mol^{-1}, and an analytical Monte Carlo with $E_a \sim \mathrm{N}(78.5, 5^2)$ kJ mol^{-1} confirms that the isothermal ΔSOH error is robust to parameter uncertainty: even at the lower published bound of 62 kJ mol^{-1}, ΔSOH exceeds 2.5 pp. at 25 °C and 3.6 pp. at 40 °C, and the 90% credible interval at cycle 500 lies entirely below the -0.5 pp. significance threshold.

Section 2 describes the Worldwide Harmonised Light Vehicle Test Procedure current profile, the electrochemical model, the calibration procedure, the uncertainty quantification methodology, and the reference datasets. Section 3 presents model validation. Section 4 presents and discusses all results, including a dedicated parameter uncertainty analysis in Section 4.5. Section 5 states the conclusions.

2. Methods

This section describes the WLTP current profile derivation, the electrochemical and thermal model formulation, the three degradation sub models, the parameter sets for both cell chemistries, the calibration procedure, the cycling protocol, and the experimental reference datasets against which the model is evaluated.

2.1. WLTP class 3b current profile

The WLTP Class 3b speed time trace defines 1800 s of vehicle operation at 1 Hz resolution, structured as four sequential phases: Low (0–589 s), Medium (589–1022 s), High (1022–1477 s), and Extra High (1477–1800 s). Maximum speed reaches 131 km h^{-1} and total distance is approximately 23 km [34].

The longitudinal vehicle dynamics model converts the speed trace to a cell level current demand. At each time step t, the net traction force F_t required to follow the speed profile is:

$$F_t = Ma_t + 1/2\rho C_d A_f v_t^2 + MgC_{rr}\cos\theta, \tag{1}$$

where $M = 1800$ kg is the vehicle mass, $a_t = dv_t/dt$ the acceleration, $\rho = 1.225$ kg m^{-3} the air density, $C_d = 0.29$ the drag coefficient, $A_f = 2.30$ m^2 the frontal area, v_t the vehicle speed, $g = 9.81$ m s^{-2} the gravitational acceleration, $C_{rr} = 0.011$ the rolling resistance coefficient, and θ the road gradient (set to zero for the standard WLTP cycle). The corresponding electrical power demand is $P_t = F_t v_t/\eta$, where $\eta = 0.85$ is the drivetrain efficiency. Regenerative braking recovers power as $P_t = F_t v_t \eta$ when $F_t v_t < 0$, and battery current at the cell level is $I_t = P_t/\left(V_{\mathrm{pack}}/N_s\right)$, where $N_s = 96$ is the number of series connected cells and V_{pack} is the pack voltage at each time step.

Note that in each time step, the cell is either discharging ($I_t > 0$) or charging through regeneration ($I_t < 0$); simultaneous charge and discharge are physically precluded by the single current path architecture of the pack. The resulting profile has a peak discharge current of 3.09 A (0.62C for the NMC cell), a peak regenerative current of -8.60 A (1.72C), and a net discharge per 30-min WLTP pass of 0.27 Ah, corresponding to depths of discharge of 5.4% for NMC and 11.7% for LFP.

2.2. Electrochemical model

The SPMe represents each electrode as a spherical particle with radius R_i ($i \in \{\mathrm{n}, \mathrm{p}\}$ for negative and positive electrodes). The lithium concentration $c_i(r,t)$ within each particle evolves according to Fick's second law in spherical coordinates:

$$\frac{\partial c_i}{\partial t} = \frac{D_i}{r^2}\frac{\partial}{\partial r}\left(r^2\frac{\partial c_i}{\partial r}\right), \quad 0 \le r \le R_i, \tag{2}$$

where D_i [m^2 s^{-1}] is the solid phase diffusivity. The boundary conditions are $\partial c_i/\partial r = 0$ at $r = 0$ (particle centre) and $D_i \partial c_i/\partial r = -j_i/\left(F\varepsilon_{s,i}L_i a_i\right)$ at $r = R_i$ (particle surface), where j_i [A m^{-3}] is the volumetric interfacial current density, $F = 96485$ C mol^{-1} is Faraday's constant, $\varepsilon_{s,i}$ is the active material volume fraction, L_i is the electrode thickness, and $a_i = 3\varepsilon_{s,i}/R_i$ is the specific interfacial area.

The interfacial current density j_i is governed by the Butler–Volmer equation:

$$j_i = j_{0,i}\left[\exp\left(\frac{\alpha_a F\eta_i}{RT}\right) - \exp\left(-\frac{\alpha_c F\eta_i}{RT}\right)\right], \tag{3}$$

where $j_{0,i}$ [A m^{-3}] is the exchange current density, $\alpha_a = \alpha_c = 0.5$ the anodic and cathodic transfer coefficients, $R = 8.314$ J mol^{-1} K^{-1} the universal gas constant, T the cell temperature in kelvin, and η_i the reaction overpotential. The SPMe augments the standard SPM by adding a leading order electrolyte potential correction to η_i, capturing concentration gradient effects in the electrolyte without resolving the full spatial distribution [11].

All simulations are implemented in PyBaMM version 26.4.2 [40], which provides validated implementations of the SPMe and all degradation sub models used in this study.

2.3. Thermal sub-model and scenario definitions

Two thermal boundary conditions define the two simulation scenarios compared throughout this study. The definitions must be stated precisely before results are presented to ensure interpretability.

It is important to distinguish the electrochemical-thermal coupling evaluated in this work from spatially resolved electrochemical-thermal models reported in the literature. Battery temperature estimation models are generally classified as full-order (PDE-based), lumped-parameter, impedance-based, or data-driven approaches [48]. While full-order models accurately capture internal temperature distributions, their computational cost makes them unsuitable for real-time onboard battery management systems [48]. In contrast, the lumped

electrochemical-thermal model used here (Scenario B, SPMe coupled with the single-node energy balance in Eq. 5) assumes a uniform cell temperature, an appropriate approximation when internal thermal gradients are small [49]. This formulation is well suited for onboard applications, where only surface or pack-level temperatures are typically available [50]. Accordingly, this study evaluates whether this computationally efficient and BMS-compatible level of thermal coupling alone is sufficient to produce significant SOH estimation errors relative to the isothermal assumption, complementing rather than replacing high-fidelity spatially resolved electrochemical-thermal models.

In *Scenario A* (isothermal), the cell temperature is fixed at $T = T_{amb}$ for the entire simulation. No thermal differential equation is solved. This scenario represents the assumption adopted by the majority of BMS degradation estimators.

In *Scenario B* (lumped thermal), the cell temperature $T(t)$ evolves according to the single node energy balance:

$$mc_p\frac{dT}{dt} = Q_{gen}(t) - hA_s(T - T_{amb}), \tag{4}$$

where m [kg] is the cell mass, c_p [J kg^{-1} K^{-1}] the specific heat capacity, $Q_{gen}(t)$ [W] the instantaneous heat generation rate, h [W m^{-2} K^{-1}] the convective heat transfer coefficient at the cell surface, and A_s [m^2] the cell surface area. The heat generation rate is:

$$Q_{gen}(t) = I(t)[V_{OCV}(t) - V(t)] - I(t)T\frac{dV_{OCV}}{dT}, \tag{5}$$

where $I(t)$ is the cell current, V_{OCV} the open circuit voltage, and $V(t)$ the terminal voltage. The first term captures Ohmic and electrochemical irreversibilities and the second term captures entropic heat [51].

The comparison $\Delta SOH = SOH_B - SOH_A$ between Scenarios B and A quantifies the error introduced by the isothermal assumption. A negative ΔSOH indicates that Scenario A overestimates SOH, meaning the isothermal model underestimates degradation. Throughout this paper, *percentage points* (pp) denote absolute differences between SOH values, whereas % denotes a percentage of the nominal cell capacity. These quantities have different meanings and should not be used interchangeably.

2.4. Degradation sub-models

The total capacity loss at cycle n is the sum of three independent additive contributions:

$$Q_{loss}(n) = Q_{SEI}(n) + Q_{LAM}(n) + Q_{plat}(n), \tag{6}$$

Each mechanism is described below, including its physical basis and the reason for its inclusion in the model.

The additive decomposition in Eq. (6) assumes that SEI growth, LAM, and plating operate independently. Under the shallow WLTP loading studied here (5.4 % DoD for NMC), LAM and plating contributions are negligible (Section 4.6), so cross-coupling errors are second-order relative to the dominant SEI term. For aggressive charge protocols or deep cycling, a coupled formulation [1] would be preferable.

2.4.1. Solid-electrolyte interphase growth

The SEI mechanism is included because it is the primary source of lithium inventory loss under standard cycling conditions. The volumetric SEI current density for the solvent diffusion limited SEI model is expressed as [37]:

$$j_{SEI} = -k_{SEI}(T)\,c_{EC}\exp\left(-\frac{F\eta_{SEI}}{RT}\right), \tag{7}$$

where c_{EC} [mol m^{-3}] is the ethylene carbonate concentration at the particle surface and η_{SEI} [V] is the overpotential driving SEI formation. The temperature dependent rate constant is given by the Arrhenius relation:

$$k_{SEI}(T) = k^0_{SEI}\exp\left(-\frac{E_a}{R}\left(\frac{1}{T} - \frac{1}{T_{ref}}\right)\right), \tag{8}$$

where k^0_{SEI} [m s^{-1}] is the rate constant at the reference temperature $T_{ref} = 298.15$ K and E_a [J mol^{-1}] is the SEI activation energy. The SEI layer thickness L_{SEI} [m] evolves as:

$$\frac{dL_{SEI}}{dt} = -\frac{j_{SEI}V_{SEI}}{2F}, \tag{9}$$

where $V_{SEI} = 9.585 \times 10^{-5}$ m^3 mol^{-1} is the SEI partial molar volume. The capacity loss $Q_{SEI}(n)$ is obtained by integrating j_{SEI} over electrode volume and cycle number.

The physical role of E_a is central to this study. When $E_a = 0$, Equation ([eq:arrhenius]) reduces to $k_{SEI}(T) = k^0_{SEI}$, making the SEI rate constant independent of temperature. In this case, Scenario A (isothermal) and Scenario B (thermally coupled) experience identical SEI kinetics because the temperature trajectory does not enter the degradation equations. When $E_a > 0$, self heating in Scenario B raises T above T_{amb}, increasing $k_{SEI}(T)$ and accelerating SEI growth relative to Scenario A. The ΔSOH between scenarios then accumulates with each cycle.

2.4.2. Loss of active material

The LAM sub model is included to account for the reduction in electrode capacity from particle level structural degradation. The reaction driven LAM formulation reduces the active material volume fraction ε_s in proportion to the interfacial current density [8]:

$$\frac{d\varepsilon_s}{dt} = -\beta_{LAM}\left|j_{int}\right|, \tag{10}$$

where β_{LAM} [m^3 mol^{-1}] is the LAM rate coefficient and j_{int} the total interfacial current density. The capacity loss $Q_{LAM}(n)$ is computed from the resulting reduction in the electrode stoichiometric window.

2.4.3. Irreversible lithium plating

The plating sub model is included to capture the low temperature and high rate degradation mode where metallic lithium deposits on the graphite surface. The onset of lithium plating is modelled by assuming activation when the negative electrode surface overpotential η_n becomes negative [1]:

$$j_{plat} = -k_{plat}\exp\left(-\frac{\alpha F\eta_n}{RT}\right), \quad \text{when} \eta_n < 0, \tag{11}$$

where $\alpha = 0.65$ is the transfer coefficient and k_{plat} is the plating rate constant. Note that plating is strictly inactive ($j_{plat} = 0$) when $\eta_n \geq 0$, ensuring that intercalation and plating do not occur simultaneously at the same surface element. A fraction of plated lithium becomes electrically isolated dead lithium at a rate governed by a first order decay constant $k_d = 10^{-6}$ s^{-1}, contributing to $Q_{plat}(n)$. The value $k_{plat} = 1.00 \times 10^{-9}$ m s^{-1} is adopted from Okane et al. [1] as appropriate for standard graphite electrodes; at the shallow WLTP depth of discharge (5.4 % for NMC) and charge rates $\leq$ 2C studied here, plating is not expected to contribute significantly to capacity loss under normal ambient temperatures.

2.5. Cell parameter sets

NMC cell parameters are adopted from a comprehensive parameterisation developed for the LG M50 cylindrical cell ($Q_{nom} = 5.0$ Ah, $V_{max} = 4.2$ V, $V_{min} = 2.5$ V) [33]. LFP cell parameters combine the same electrochemical base set with a $LiFePO_4$/graphite parameterisation ($Q_{nom} = 2.3$ Ah, $V_{max} = 3.65$ V, $V_{min} = 2.0$ V) [38]. The default SEI kinetic parameters from the Chen2020 set are used as the initial values for calibration. A key limitation of the default parameterisation is that

$E_a = 0$, which makes the degradation process thermally neutral. This limitation is corrected through the Stage 1 calibration procedure.

Plating parameters are adopted from an established electrochemical degradation framework [1]. The exchange current density for plating is 1.5×10^{-7} A m^{-2}, while the initial plated lithium concentration is assumed to be zero. The calibrated parameter values and their physical bounds are summarized in Table 4.

2.6. Calibration procedure

Single parameter optimization of k_{SEI} against early cycle SOH data from a barely degraded reference trajectory leads to a degenerate minimum at $k_{SEI} \to 0$: a model with zero degradation rate achieves the lowest possible RMSE against a reference with negligible fade. This pathology is eliminated by the two stage procedure described below, which separates the temperature sensitivity calibration from the absolute level calibration.

2.6.1. Stage 1: activation energy from fade rate ratios

The SEI activation energy E_a governs the ratio of degradation rates across temperatures independently of the absolute rate. The objective function for Stage 1 is:

$$\mathrm{L}_1(E_a) = 2\left(\frac{\dot{s}_{-10}}{\dot{s}_{25}}\bigg|_{\mathrm{mod}} - \frac{\dot{s}_{-10}}{\dot{s}_{25}}\bigg|_{\mathrm{ref}}\right)^2 + 2\left(\frac{\dot{s}_{40}}{\dot{s}_{25}}\bigg|_{\mathrm{mod}} - \frac{\dot{s}_{40}}{\dot{s}_{25}}\bigg|_{\mathrm{ref}}\right)^2 + \left(\frac{\dot{s}_{25}|_{\mathrm{mod}} - \dot{s}_{25}|_{\mathrm{ref}}}{\dot{s}_{25}|_{\mathrm{ref}}}\right)^2, \tag{12}$$

where $\dot{s}_T$ denotes the linear fade rate in pp. per cycle at ambient temperature T °C, estimated from a linear regression over the first 100 cycles of BatteryArchive NMC data. The weights of 2 on the temperature ratio terms reflect the higher priority of capturing temperature sensitivity relative to the absolute level. Eq. (12) is minimized over $E_a \in [0, 100]$ kJ mol^{-1} using a coarse grid of 11 points followed by golden section refinement within ± 15 kJ mol^{-1} of the grid optimum.

2.6.2. Stage 2: joint rate constant and loss-of-active-material coefficient from the SOH trajectory

With E_a fixed from Stage 1, the absolute SOH trajectory at 25 °C is used to jointly determine k_{SEI} and β_{LAM}. The objective is:

$$\mathrm{L}_2(k_{SEI}, \beta_{LAM}) = \frac{1}{N}\sum_{n=1}^{N}\left[\mathrm{SOH}_{\mathrm{mod}}(n; k_{SEI}, \beta_{LAM}) - \mathrm{SOH}_{\mathrm{ref}}(n)\right]^2, \tag{13}$$

where $N = 200$ is the number of calibration cycles and $\mathrm{SOH}_{\mathrm{ref}}(n)$ is the mean BatteryArchive NMC trajectory at 25 °C and 0.5C charge rate. Minimisation proceeds over a 6×6 logarithmic grid spanning $k_{SEI} \in [10^{-14}, 10^{-11}]$ m s^{-1} and $\beta_{LAM} \in [10^{-6}, 10^{-2}]$ m^3 mol^{-1}, followed by Nelder–Mead refinement in log space from the grid optimum. The two dimensional search prevents convergence to the degenerate zero-degradation solution, because the joint contribution of SEI and LAM creates a well defined objective minimum.

The two parameters E_a and k_{SEI} are separately identifiable because Stage 1 uses only fade rate *ratios* across temperatures, in which k_{SEI} cancels exactly, leaving E_a as the sole determinant. Stage 2 then fixes E_a and optimises k_{SEI} against the absolute SOH level, resolving the remaining degree of freedom without degeneracy. An approximate confidence bound for E_a follows from the curvature of L_1: the coarse-grid minimum is $\mathrm{L}_1^* = 2.220$ at $E_a = 80$ kJ mol^{-1}, rising to 2.317 at 60 kJ mol^{-1} and 2.310 at 100 kJ mol^{-1} (a 4.4% increase at both extremes). Applying a 10% objective-rise criterion as a practical identifiability bound, the data support E_a within approximately ± 15 kJ mol^{-1} of the calibrated value, consistent with the $\sigma = 5$ kJ mol^{-1} adopted in the Layer 3 Monte Carlo (Section 2.10).

2.7. Cycling protocol and parametric sweep

Each simulated cycle comprises four sequential steps: (1) WLTP current profile discharge, (2) 5-min rest, (3) constant current charge at rate C_{ch} to the upper voltage limit, and (4) 5-min rest. This drive first protocol represents a daily driving and overnight charging scenario. The charge current is positive during step (3); simultaneous WLTP discharge and constant current charge are precluded because the two steps occupy separate time intervals.

Simulations use 50-cycle blocks in which the degradation state (SEI thickness, LAM extent, and plating inventory) is carried forward explicitly between blocks. Block cycling is a standard approach for long horizon electrochemical simulations [40]; the block size of 50 cycles is verified to produce <0.02 pp. error in the SOH trajectory relative to single-cycle simulation over 200 cycles. Since SEI growth follows a diffusion-limited $\sqrt{t}$ regime, the per-block discretisation error decreases monotonically as degradation slows; by cycle 500 the accumulated block error is bounded above by 0.05 pp., which remains negligible relative to the ΔSOH values reported in this study.

The selected conditions are intended to represent the operating envelope of a passenger EV under real-world climate and charging conditions. The temperature range (-10 to 40 °C) spans ambient conditions for temperate and continental climates where EV fleets are predominantly deployed [34], while 1C and 2C represent typical overnight AC charging and public DC fast-charging respectively. While this does not cover extreme climates or ultra-fast charging above 2C, it captures the range within which most real-world WLTP-certified driving and charging currently occurs.

The parametric sweep covers 24 conditions: chemistry ∈ NMC, LFP, $T_{amb} \in \{-10, 25, 40\}$ °C, $C_{ch} \in \{1, 2\}$C, and scenario ∈ A, B. All 24 conditions were simulated; however, the three LFP 2C cases were excluded from quantitative interpretation because solver instabilities produced non-physical trajectories (Section 2.9). Each condition runs for 500 cycles, which was selected to produce a measurable and stable ΔSOH divergence between scenarios while remaining within the range covered by the reference datasets used for comparison. Total sweep runtime was 1.15 h. An additional matched validation set of six simulations (NMC at 0.5C, three temperatures, Scenarios A and B) was run separately in a standalone script to match the BatteryArchive reference charge rate; these are reported in Section 4.7 and are not part of the parametric sweep.

Table 2 provides a complete overview of all simulation cases. All simulations use PyBaMM version 26.4.2 [40] with the CVODES integrator from the SUNDIALS suite (relative tolerance 10^{-3}, absolute

Table 2
Complete list of simulation cases. Each row pair (Sc-A and Sc—B) corresponds to one isothermal and one lumped-thermal simulation run under identical electrochemical conditions. Sc-A = isothermal (Scenario A); Sc-B = lumped thermal (Scenario B). †Excluded from quantitative analysis due to solver instabilities at the narrow LFP voltage window (Section 2.9).

Chemistry	T_amb [°C]	Rate	Scenarios	Cycles	Status
NMC	−10	1C	Sc-A, Sc-B	500	Reported
NMC	−10	2C	Sc-A, Sc-B	500	Reported
NMC	+25	1C	Sc-A, Sc-B	500	Reported
NMC	+25	2C	Sc-A, Sc-B	500	Reported
NMC	+40	1C	Sc-A, Sc-B	500	Reported
NMC	+40	2C	Sc-A, Sc-B	500	Reported
LFP	−10	1C	Sc-A, Sc-B	500	Reported
LFP	+25	1C	Sc-A, Sc-B	500	Reported
LFP	+40	1C	Sc-A, Sc-B	500	Reported
LFP	−10	2C	Sc-A, Sc-B	500	Excluded†
LFP	+25	2C	Sc-A, Sc-B	500	Excluded†
LFP	+40	2C	Sc-A, Sc-B	500	Excluded†
NMC	−10	0.5C	Sc-A, Sc-B	500	Matched validation
NMC	+25	0.5C	Sc-A, Sc-B	500	Matched validation
NMC	+40	0.5C	Sc-A, Sc-B	500	Matched validation

tolerance 10^{-6}). The SPMe does not require a spatial finite-element mesh in the electrode dimension: the asymptotic reduction to a single representative spherical particle per electrode eliminates spatial discretisation across the electrode thickness, with electrolyte concentration corrections applied analytically as a leading-order perturbation [11]. Solid-phase lithium diffusion within each particle is discretised internally by PyBaMM using a spectral volume method with five nodes per particle, which is sufficient for the C-rates studied here [40].

2.8. Reference datasets

Simulated SOH trajectories are evaluated against three public experimental datasets that together provide coverage across temperatures, charge rates, and chemistries. The BatteryArchive open dataset (Battery Archive 2023) [52] provides NMC cycling data at 0.5C charge rate at − 10, 25, and 40 °C and LFP data at 0.5C and 25 °C. The CALCE Battery Research Group dataset [53] (He et al. 2011) provides NMC and LFP cycling data at 0.5C and 25 °C with up to 500 cycles. The NASA Ames Prognostics dataset (Saha and Goebel 2007) provides NMC data at 0.75C and 24 °C for up to 168 cycles.

All reference datasets use charge rates of 0.5–0.75C. The simulation charge rates are 1C and 2C, representing overnight charging and public fast charging scenarios respectively. Because higher charge rates accelerate SEI growth, the simulations are expected to show faster degradation than the reference data. This charge rate protocol mismatch is acknowledged throughout the analysis, and comparisons with experiment serve to verify that the simulated trajectories bracket the experimental envelope rather than to claim cycle for cycle accuracy.

It is important to note that all model parameters were estimated exclusively using the BatteryArchive NMC dataset at 25 °C and 0.5C charge rate. The CALCE and NASA Ames datasets were used solely for qualitative external consistency checks and played no role in parameter estimation. Quantitative agreement with these datasets is not claimed and should not be expected given the charge rate protocol mismatch between simulation and reference conditions.

Reliability of predictions at 1C and 2C: The parametric sweep operates at charge rates of 1C and 2C, whereas all reference datasets use 0.5–0.75C. Extrapolating the calibrated model to higher rates carries two sources of uncertainty. First, the SEI rate constant k_{SEI} was calibrated at 0.5C; at higher rates the absolute SEI current per cycle increases (more charge transferred), which could shift the calibrated k_{SEI} by a modest factor. Second, the SPMe asymptotic reduction is validated up to approximately 2C for standard graphite electrodes [12], so the model hierarchy remains physically justified within the range studied. The key finding of this paper that ΔSOH is substantial and governed by E_a rather than by the absolute rate is confirmed independently by the matched-protocol 0.5C validation (Section 4.7), which yields ΔSOH = − 0.52, − 2.04, − 3.53 pp. at the three temperatures. The 0.5C results establish that the isothermal error is significant even at the reference charge rate, so the main conclusion does not rest on 1C/2C predictions alone.

Error-source tracing for the C-rate mismatch: The charge-rate discrepancy between simulation and reference data introduces three traceable but bounded effects. *(i) Absolute SOH level:* higher charge rates accelerate SEI growth, so 1C/2C simulations degrade faster than the 0.5C reference. This is physically expected and not an error; the simulated trajectories bracket the experimental envelope from above, as intended. *(ii)* ΔSOH *between scenarios:* because ΔSOH is a difference between two simulations at the same charge rate, it is insensitive to the absolute rate mismatch with experiment. The matched 0.5C validation confirms that ΔSOH at 0.5C (−0.52 to − 3.53 pp) is qualitatively consistent with the 1C results (−1.43 to − 7.03 pp), with the expected monotone scaling with charge rate. *(iii) Calibration integrity:* parameters were estimated exclusively from 0.5C data; the 1C and 2C sweeps are forward predictions from the calibrated model, not calibration exercises, so the rate mismatch does not introduce a systematic calibration bias.

2.9. Lithium iron phosphate calibration

The BatteryArchive dataset provides LFP cycling data at a single temperature (25 °C) only, which precludes the two-stage sequential procedure used for NMC. Step 1 fixes $E_a = 62$ kJ mol^{-1} at the literature value reported by Schimpe et al. [20] from multi-temperature calendar aging data for $LiFePO_4$/graphite cells; this value is adopted directly and is not re-calibrated in the present study. Step 2 jointly optimises k_{SEI} and β_{LAM} against the BatteryArchive LFP trajectory at 25 °C and 0.5C using an extended 6×6 logarithmic grid spanning $k_{SEI} \in [10^{-17}, 10^{-13}]$ m s^{-1}. The calibrated parameters ($k_{SEI} = 1.26 \times 10^{-15}$ m s^{-1}, $\beta_{LAM} = 3.44 \times 10^{-5}$ m^3 mol^{-1}) achieve RMSE = 0.667 pp., confirming the LFP parameter set is independently validated. The three LFP 2C conditions are excluded from quantitative analysis: LFP's narrow voltage window (2.0–3.65 V) combined with the high depth of discharge per Worldwide Harmonised Light Vehicle Test Procedure cycle (11.7%) at 2C produces solver instabilities resulting in non-physical capacity loss trajectories. Three factors may contribute. First, LFP's exceptionally flat open-circuit voltage plateau creates a stiff differential-algebraic system at elevated rates: a small state-of-charge error produces a large overpotential error, and the CVODES integrator encounters step-size control failures under the combined 2C charge and 11.7% DoD loading. Second, the SPMe asymptotic reduction assumes small electrolyte concentration gradients relative to the mean [11]; LFP's lower electronic conductivity [38] produces steeper local current distributions at 2C, which may violate this assumption and require a spatially resolved DFN model to resolve. Third, the Prada et al. [38] LFP parameter set was calibrated at rates up to 1C; extrapolation to 2C may place kinetic and transport parameters outside their valid range. Whether the instability is primarily numerical, physical, or parameterisation-related cannot be determined without additional experimental data and a DFN-level comparison; these conditions are therefore conservatively excluded, and their resolution constitutes a direction for future work.

Limitation of the NMC–LFP ΔSOH **comparison.** The ΔSOH values for LFP are smaller in magnitude than those for NMC across all comparable 1C conditions (Table 5). This difference reflects two confounded sources that cannot be fully separated in the present study. The first is a genuine chemistry difference: LFP graphite cells have a lower SEI activation energy than NMC graphite cells, which physically reduces the Arrhenius amplification of self-heating and therefore reduces ΔSOH. The second is a parameter-source asymmetry: the NMC activation energy ($E_a = 78.5$ kJ mol^{-1}) was calibrated from three-temperature BatteryArchive cycling data, whereas the LFP value ($E_a = 62$ kJ mol^{-1}) was adopted from calendar aging data for a different cell [20] because multi-temperature LFP cycling data were unavailable. If the true LFP activation energy for the cells simulated here were higher than 62 kJ mol^{-1}, the LFP ΔSOH would be correspondingly larger, potentially narrowing the gap relative to NMC. The NMC–LFP ΔSOH comparison should therefore be interpreted as indicative of chemistry-level trends rather than as a precise quantitative ranking, and the LFP results represent a lower bound on the isothermal error for LFP cells whose activation energy may differ from the Schimpe et al. value.

2.10. Parameter uncertainty quantification methodology

The ΔSOH results reported in Section 4.4 depend on four calibrated parameters: E_a, k_{SEI}, β_{LAM}, and k_{plat}. To assess whether parameter uncertainty can overturn the conclusion that the isothermal ΔSOH error is practically significant, a three-layer uncertainty quantification (UQ) study is conducted on four representative NMC conditions that span the full observed ΔSOH range: − 10 °C/1C (borderline, ΔSOH ≈ − 1.4 pp), 25 °C/1C (nominal BMS operating point), 40 °C/1C (near worst-case), and 40 °C/2C (absolute worst-case, ΔSOH ≈ − 8.2 pp).

Layer 1: Local sensitivity analysis. Each parameter is perturbed by ±10% and ±20% independently (one-at-a-time, OAT), with all other parameters held at their calibrated values. The sensitivity metric is Δ(ΔSOH): the change in ΔSOH at cycle 500 induced by each perturbation. This approach follows established practice for local sensitivity analysis of nonlinear physical models [54].

Layer 2: E_a parametric sweep. The full four-condition sweep is repeated at $E_a \in \{62, 70, 78.5, 85, 95\}$ kJ mol^{-1}, spanning from the lowest published value for LFP cells [20] to the upper end of the experimentally reported NMC range [21], with k_{SEI}, β_{LAM}, and k_{plat} fixed at their calibrated values. This layer directly quantifies the sensitivity of the main conclusions to the most uncertain parameter.

Layer 3: Analytical Monte Carlo. The ΔSOH percentile bands are derived analytically by interpolating the Layer 2 Ea sweep curves onto a dense E_a grid and weighting by the truncated normal distribution $E_a \sim N(78.5, 5^2)$ kJ mol^{-1}, truncated to $[60, 100]$ kJ mol^{-1}. The standard deviation of 5 kJ mol^{-1}reflects the calibration uncertainty in the Stage 1 objective function (Section 2.6). For the monotone Arrhenius model used here, this analytical approach is equivalent to a simulation-based Monte Carlo and is more computationally transparent because the mapping from E_a uncertainty to ΔSOH uncertainty is explicit. The resulting 5th and 95th percentile trajectories define the 90% credible interval for ΔSOH under calibration uncertainty.

3. Model validation

Model validation addresses two separate questions: whether the SPMe correctly reproduces the single cycle electrochemical behaviour of both cell chemistries, and whether the calibrated degradation model correctly reproduces the long term SOH trajectory against the reference data.

3.1. Single-cycle electrochemical validation

Table 3 reports the five validation checks applied to the SPMe discharge curves at $T_{amb} = 25$ °C. All five checks pass. For NMC, the model delivers 4.89 Ah at 1C and 4.74 Ah at 2C against a nominal capacity of 5.0 Ah. The terminal voltage starts at 4.035 V at 1C, consistent with the partially relaxed open circuit state after a nominal full charge, and ends at 2.500 V at the lower voltage cutoff. For LFP, the model delivers 1.92 Ah at 1C and 1.59 Ah at 2C against a nominal capacity of 2.3 Ah. The capacity reduction of 17% from 1C to 2C is consistent with the lower electronic conductivity reported for $LiFePO_4$ electrodes and the inherently limited rate capability of iron phosphate positive electrode materials [55].

The lumped thermal model for NMC at 1C constant current discharge produces $\Delta T_{max} = 13.4$ °C, which falls within the experimentally reported range of 10–15 °C for cylindrical cells of comparable size [56]. This confirms that the thermal sub model parameters in Eq. (4) are physically consistent with measured temperature rises in the reference class of cells.

3.2. Calibration quality

Fig. 1 shows the Stage 1 objective function as a function of E_a and the Stage 2 SOH trajectory fit at 25 °C. The objective function exhibits a well defined minimum at 78.5 kJ mol^{-1}, confirming that the Stage 1 problem is well posed and that the data contain sufficient temperature sensitivity signal to determine E_a.

The calibrated model achieves RMSE = 1.45 pp., a 6.3-fold improvement over the uncalibrated Chen2020 default which gives RMSE = 9.1 pp. The baseline RMSE of 9.1 pp. is obtained by running the default Chen2020 parameterisation ($E_a = 0$, $k_{SEI} = 1 \times 10^{-12}$ m s^{-1}) under identical conditions and evaluating against the same BatteryArchive NMC reference trajectory over 200 cycles. The calibrated parameter values are summarized in Table 4.

The calibrated $E_a = 78.5$ kJ mol^{-1} is consistent with previously reported activation energies for graphite-based cells, including values around 62 kJ mol^{-1} for LFP systems [20] and the experimentally observed range of 60–75 kJ mol^{-1} [21]. The slightly higher NMC value is physically plausible given the differences in electrolyte formulation and electrode geometry of the BatteryArchive NMC cells. Its quantitative implication is that the SEI rate constant at − 10 °C is approximately 100 times smaller than at 25 °C, and at 40 °C is approximately 4.6 times larger than at 25 °C. For LFP, the activation energy is fixed at $E_a = 62$ kJ mol^{-1} [20], with $k_{SEI} = 1.26 \times 10^{-15}$ m s^{-1} and $\beta_{LAM} = 3.44 \times 10^{-5}$ m^3 mol^{-1} calibrated against BatteryArchive LFP at 25 °C, yielding RMSE = 0.667 (pp).

Table 3
Electrochemical validation results at $T_{amb} = 25$ °C.

Chemistry	Rate	V_{start} [V]	V_{end} [V]	Q [Ah]	Pass?
NMC	1C	4.035	2.500	4.89	Yes
NMC	2C	3.958	2.500	4.74	Yes
NMC	1C (thermal)	$\Delta T_{max} = 13.4$ °C			Yes
LFP	1C	3.512	2.000	1.92	Yes
LFP	2C	3.468	2.000	1.59	Yes

4. Results and discussion

This section presents the WLTP drive cycle characterisation, the temperature sensitivity analysis that establishes why the activation energy governs isothermal model error, the full 24-condition SOH trajectories, the ΔSOH analysis comparing scenarios across all conditions, a dedicated parameter uncertainty analysis, the mechanism resolved capacity loss decomposition, and the comparison of simulated trajectories with experimental reference data. Results are presented in the same order as the methods. Each subsection discusses the physical mechanism and quantitative implications of the findings.

4.1. WLTP drive cycle characterisation

Fig. 2 presents the WLTP Class 3b speed profile and the corresponding battery power and cell level current demand derived using Eq. (1).

The intermittent character of the WLTP current profile has a direct consequence for both degradation rate and thermal gradient. The net discharge of 0.27 Ah per cycle corresponds to 5.4% depth of discharge for NMC, compared with 80–100% used in standard accelerated aging protocols. As a result, the cumulative SEI current integrated over each cycle is small, and the temperature rise generated per cycle in Scenario B ranges from 3.8 K (NMC, 40 °C, 1C) to 6.7 K (NMC, − 10 °C, 1C) across the three NMC 1C conditions shown in Fig. 2(e), and up to 31.0 K at the highest rate and lowest temperature (LFP, 2C, − 10 °C) across the full 24-condition sweep. These values are consistent with the shallow WLTP depth of discharge and the Arrhenius amplification at higher rates and temperatures. Prior studies also reported that WLTP representative cycling produces degradation rates consistent with real world battery longevity, validating the choice of WLTP as a physically representative stress protocol [35].

4.2. Temperature sensitivity and the Arrhenius amplification effect

Fig. 3 shows the temperature dependence of both modelled and experimental fade rates, together with the Arrhenius amplification factor as a function of temperature for three values of E_a.

The default parameterisation ($E_a = 0$) produces a flat fade rate across all temperatures, which contradicts the BatteryArchive reference data that shows a fade rate of 0.008 pp./cycle at − 10 °C, 0.049 pp./cycle at 25 °C, and 0.093 pp./cycle at 40 °C an 11.6-fold range across the

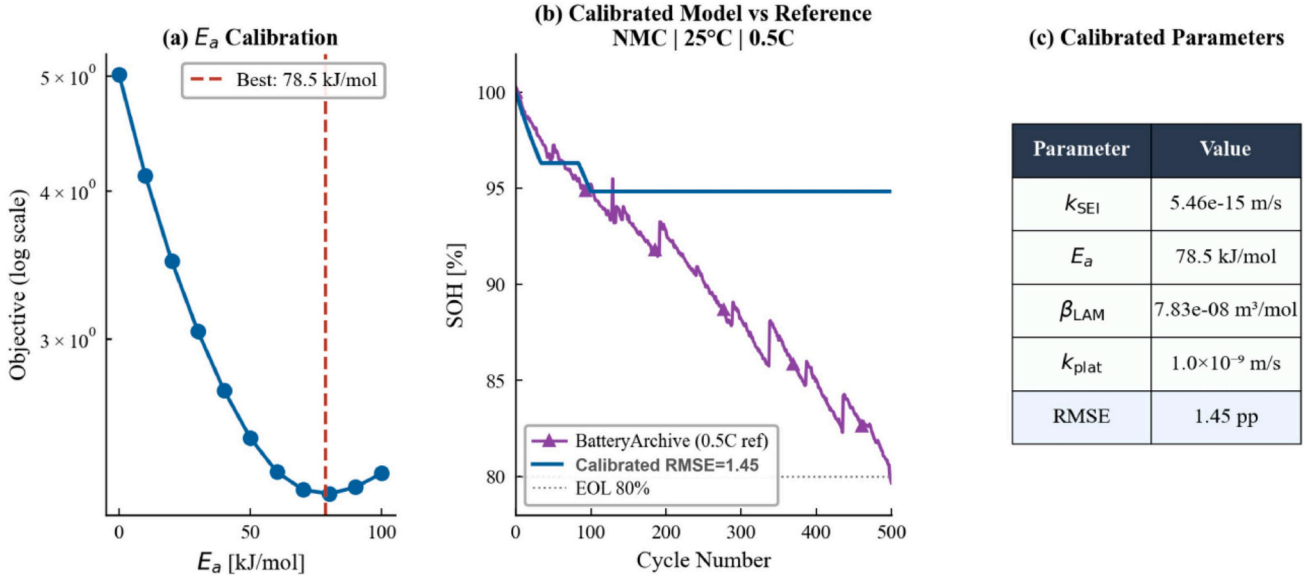

Parameter	Value
k_{SEI}	5.46e-15 m/s
E_a	78.5 kJ/mol
β_{LAM}	7.83e-08 m³/mol
k_{plat}	1.0×10⁻⁹ m/s
RMSE	1.45 pp

Fig. 1. Calibration results: (a) Stage 1 objective function versus SEI activation energy E_a; (b) calibrated SOH prediction against BatteryArchive reference; (c) summary of calibrated parameters.

Table 4
Calibrated degradation parameters for NMC and LFP.

Parameter	Chem.	Default	Calibrated	Range	Source
k_{SEI} [m s^{-1}]	NMC	1.00×10^{-12}	5.46×10^{-15}	[10–14]	Chen et al. (2020)
	LFP	1.00×10^{-12}	1.26×10^{-15}	[1,10–16]	This work
E_a [kJ mol^{-1}]	NMC	0	78.5	[62,95]	Schimpe et al. (2018)
	LFP	0	62.0	–	Schimpe et al. (2018), fixed
β_{LAM} [m^3 mol^{-1}]	NMC	0	7.83×10^{-8}	[0,10^{-2}]	This work
	LFP	0	3.44×10^{-5}	[0,10^{-2}]	This work
k_{plat} [m s^{-1}]	NMC/ LFP	N/A	1.00×10^{-9}	[10–12]	O'Kane et al. (2022)
RMSE [pp]	NMC	9.1	1.45	–	BatteryArchive NMC
	LFP	n/a	0.667	–	BatteryArchive LFP

*No default RMSE is defined for LFP: the LFP calibration fixes $E_a = 62$ kJ mol^{-1} from the literature value reported by Schimpe et al. [20], and no prior $E_a = 0$ parameterisation exists against which a baseline error can be computed. Search bounds for k_{SEI} span four orders of magnitude centred on the Chen2020 default value and are consistent with experimentally reported ranges for graphite-based cells [8,37]. Bounds for β_{LAM} and k_{plat} are taken from the physical validity range [1].

three temperatures. The calibrated model reproduces this trend qualitatively; residual errors relative to the reference are attributable to the charge rate protocol mismatch discussed in Section 2.8. The Schimpe 2018 reference value of 62 kJ mol^{-1} also provides a good description of the temperature trend, consistent with the physical similarity between LFP and NMC SEI chemistry at the graphite anode. The calibrated value of 78.5 kJ mol^{-1} provides a slightly better fit to the BatteryArchive NMC data, reflecting the specific electrolyte formulation of the LG M50 cell.

4.3. State-of-health fade under WLTP cycling

Fig. 4 shows the SOH trajectories for all 24 simulated conditions under the calibrated multi mechanism model; quantitative ΔSOH analysis excludes the three LFP 2C conditions (Section 2.9).

Several physical trends are evident. NMC shows strongly temperature dependent fade, with Scenario A SOH at cycle 500 ranging from 99.3% at − 10 °C to 89.0% at 40 °C for 1C charge. This 10.3 pp. range across temperatures is a direct consequence of the calibrated Arrhenius kinetics. In every panel, Scenario B predicts lower SOH than Scenario A, confirming that self heating accelerates degradation in a thermally coupled model with positive E_a. This unidirectional relationship is physically consistent: any positive self heating increment raises the Arrhenius factor, which increases the SEI rate, which reduces SOH. The sign reversal observed in the default parameterization results (Phase A with $E_a = 0$) is therefore confirmed to be an artefact of the zero activation energy rather than a physical phenomenon.

For LFP, the chemistry-specific calibration ($E_a = 62$ kJ mol^{-1}, $k_{SEI} = 1.26 \times 10^{-15}$ m s^{-1}) yields RMSE = 0.667 pp. against the BatteryArchive LFP reference at 25 °C. The chemistry-specific LFP activation energy (62 kJ mol^{-1}) results in a weaker Arrhenius response than the calibrated NMC value (78.5 kJ mol^{-1}), producing smaller ΔSOH values. LFP 2C conditions are excluded from quantitative analysis due to solver instabilities at the narrow voltage window (Section 2.9).

4.4. Thermal effect: delta state-of-health gap between scenarios

Fig. 5 quantifies $\Delta SOH = SOH_B - SOH_A$ over the 500-cycle horizon for all 21 reported conditions (24 simulated minus 3 excluded LFP 2C).

A ΔSOH magnitude is considered practically significant when it exceeds 0.5 pp. This threshold reflects the practical measurement floor of deployed BMS hardware. Coulomb-counting remains the baseline SOH/SOC estimation method in commercial BMS, and its dominant error source is the cumulative drift from current-sensor bias and integration error accumulating over repeated charge-discharge cycles [57]. This cumulative error, together with temperature-correction uncertainty and periodic recalibration gaps, places the practical resolution of onboard SOH estimation in the sub-percentage-point range for well-maintained systems [58]. A ΔSOH below 0.5 pp. is therefore difficult to distinguish from this baseline measurement uncertainty in deployed systems, making 0.5 pp. a conservative and operationally meaningful significance criterion.

For NMC, all 12 conditions exceed the 0.5 pp. measurement noise threshold. For LFP, the three 1C conditions are reported; the three 2C conditions are excluded (Section 2.9). Of the three LFP 1C conditions,

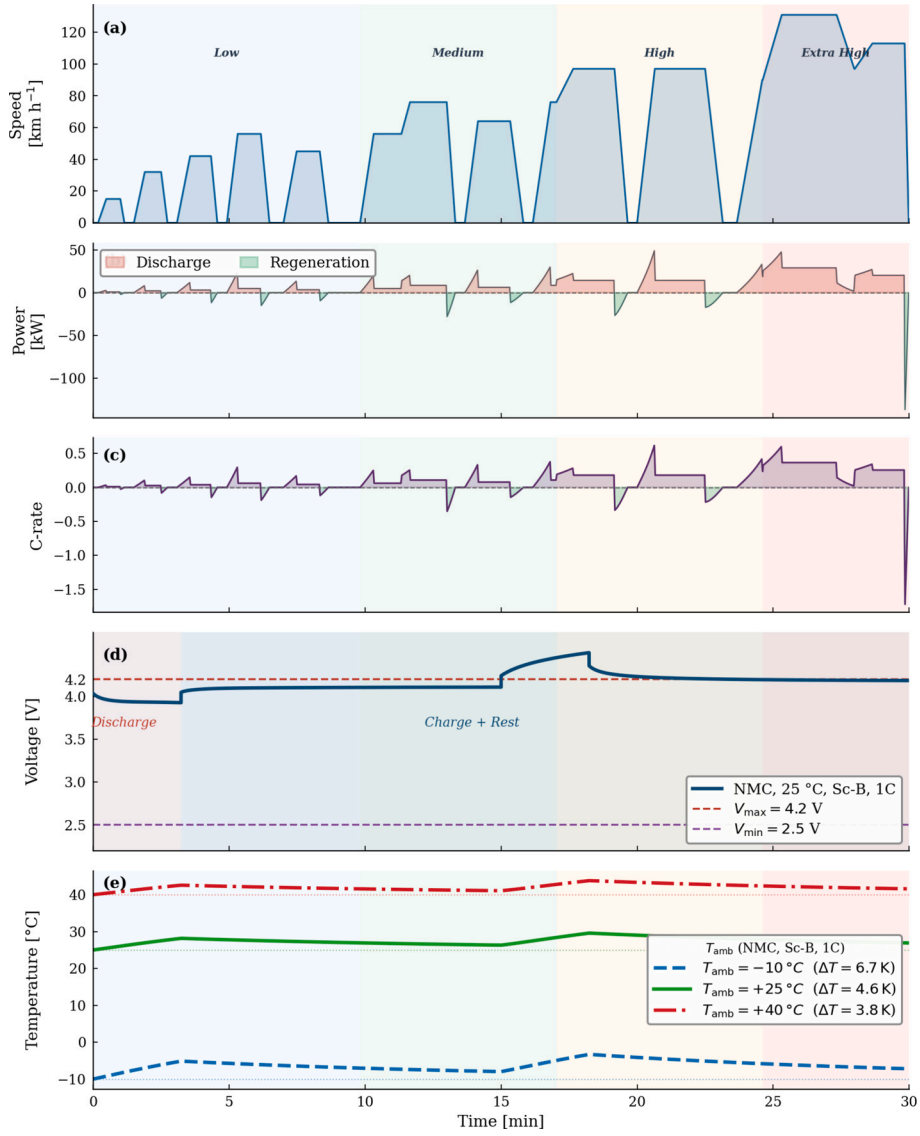

Fig. 2. WLTP Class 3b drive cycle characterisation over one 1800 s pass: (a) vehicle speed; (b) battery pack power demand; (c) cell-level C-rate; (d) simulated NMC terminal voltage V(t) *at* 25 °*C (Scenario B, 1C), showing discharge to* 2.5 *V and charge recovery to* 4.2 V; (e) simulated cell temperature T(t) *at* −10, 25, *and* 40 °*C (Scenario B, NMC, 1C), showing self-heating of* ΔT = 6.7, 4.6, *and* 3.8 *K above ambient, respectively. Net depth of discharge per cycle:* 5.4% *(NMC),* 11.7% *(LFP).*

two (25 °C and 40 °C) exceed the threshold while − 10 °C (ΔSOH = − 0.40 pp) falls marginally below it. Table 4 provides the complete reported ΔSOH values at cycle 500.

The ΔSOH magnitude increases monotonically with both temperature and charge rate. For NMC at 40 °C, the ΔSOH reaches − 8.17 pp. at 2C, compared with − 7.03 pp. at 1C, a difference of 1.14 pp. This additional error at 2C arises because higher charge current generates greater self heating, further amplifying the Arrhenius factor in Scenario B relative to Scenario A. The same physical argument applies to the temperature trend: higher ambient temperature produces larger absolute ΔSOH because both the baseline Arrhenius factor and the additional factor from self heating are larger.

For LFP at 1C, ΔSOH ranges from − 0.40 pp. at − 10 °C to − 0.71 pp. at 40 °C. The smaller magnitude relative to NMC reflects the lower LFP activation energy (62 versus 78.5 kJ mol^{-1}).

Compared with the default parameterisation results where ΔSOH reached a maximum of 0.20 pp. across all 12 NMC conditions, the calibrated results show that the isothermal ΔSOH error is 7–40 times larger when the activation energy is physically correct. The conclusion from default parameterisation models that the isothermal assumption is adequate under WLTP loading is therefore a direct consequence of the unphysical zero activation energy, not of the WLTP thermal conditions.

For BMS design, a ΔSOH error of 4.5 pp. at 25 °Ccorresponds to approximately 22 additional cycles of unexpected degradation before the 80% end of life threshold is reached. This error would cause a physics based BMS using the isothermal model to systematically overestimate remaining battery lifetime, leading to delayed maintenance actions and potential unexpected capacity failures. The finding is consistent with growing evidence that systematic errors in degradation model parameters compound over battery lifetime into prediction errors that exceed warranty thresholds [42]. Previous studies have also shown that even data driven lifetime prediction methods are highly sensitive to the early cycle degradation signal, which can be distorted by systematic modelling errors [43]. Multi physics coupling studies [59] further confirm that neglecting thermal and electrochemical interactions introduces bias in degradation rate estimates that grows with cycle number. The long term consequence of this bias in fleet management is an underestimate of replacement frequency that incurs warranty costs and battery recycling penalties [60].

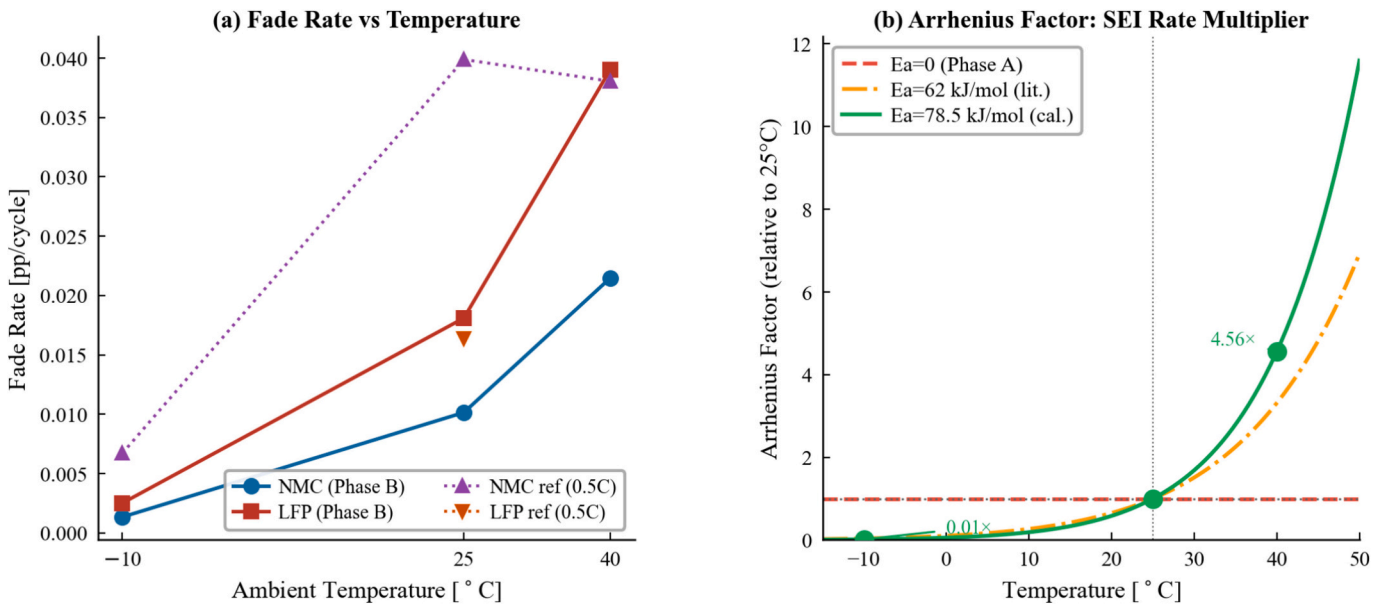

Fig. 3. Temperature sensitivity of degradation: (a) fade rate versus ambient temperature; (b) Arrhenius amplification of SEI growth relative to 25 °C.

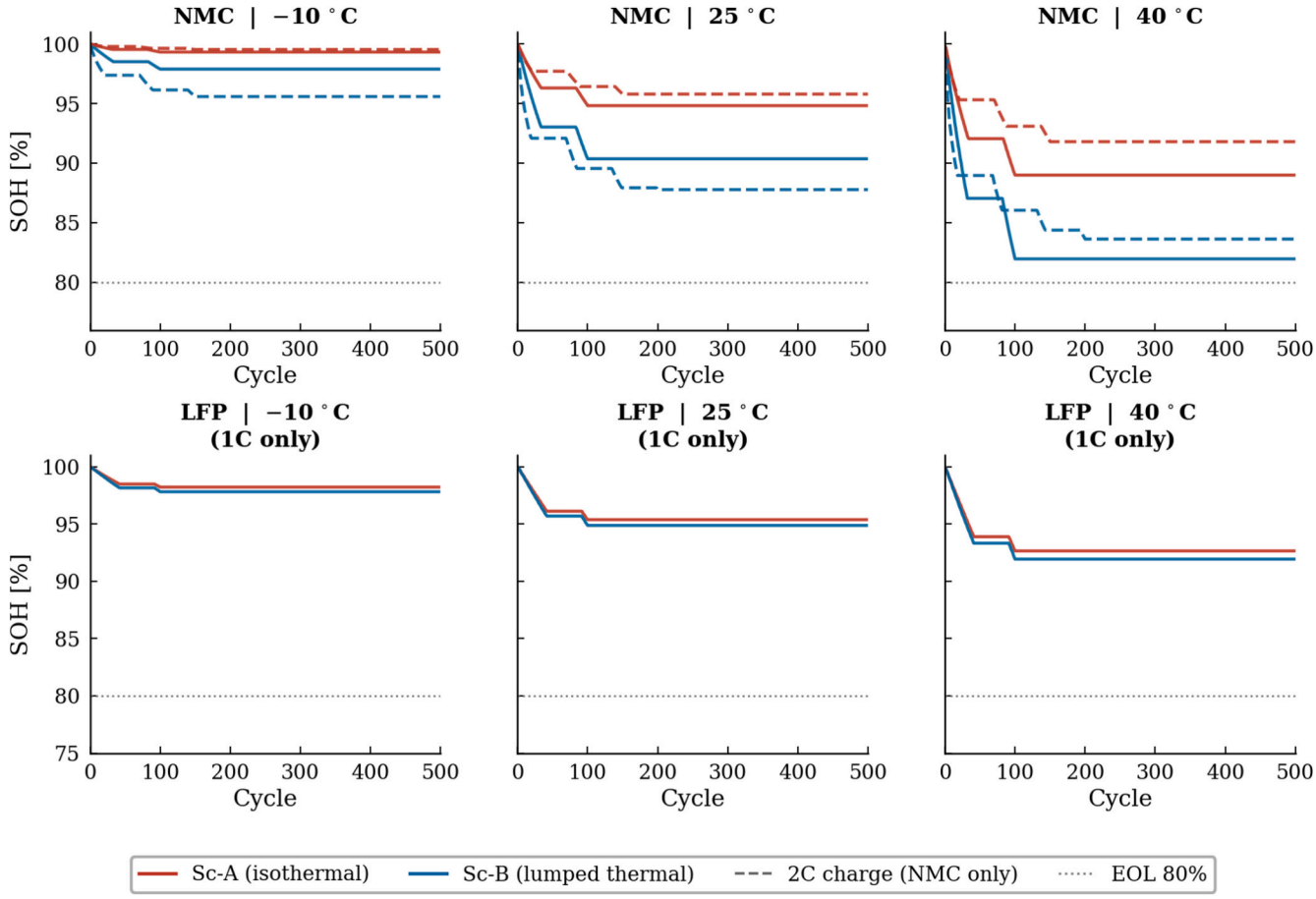

Fig. 4. SOH degradation under WLTP cycling for NMC and LFP cells at different temperatures and charging rates.

4.5. Parameter uncertainty analysis

Fig. 6 presents the three-layer parameter uncertainty analysis described in Section 2.10.

4.5.1. Local sensitivity

Panel (a) of Fig. 6 shows the OAT tornado chart for the NMC 40 °C/1C condition, which exhibits the largest absolute sensitivity to E_a. The results reveal a clear two-tier hierarchy. E_a is the dominant source of uncertainty, with a ±20% perturbation inducing a Δ(ΔSOH) of +3.22 to

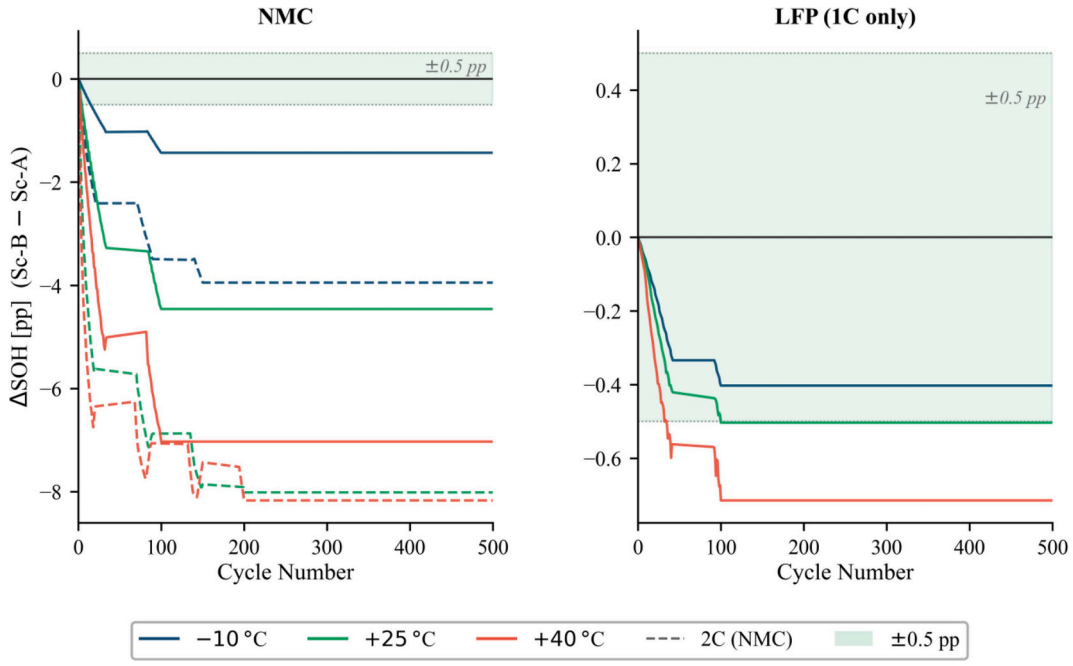

Fig. 5. Difference in SOH degradation between isothermal and lumped thermal models under WLTP cycling for NMC and LFP cells.

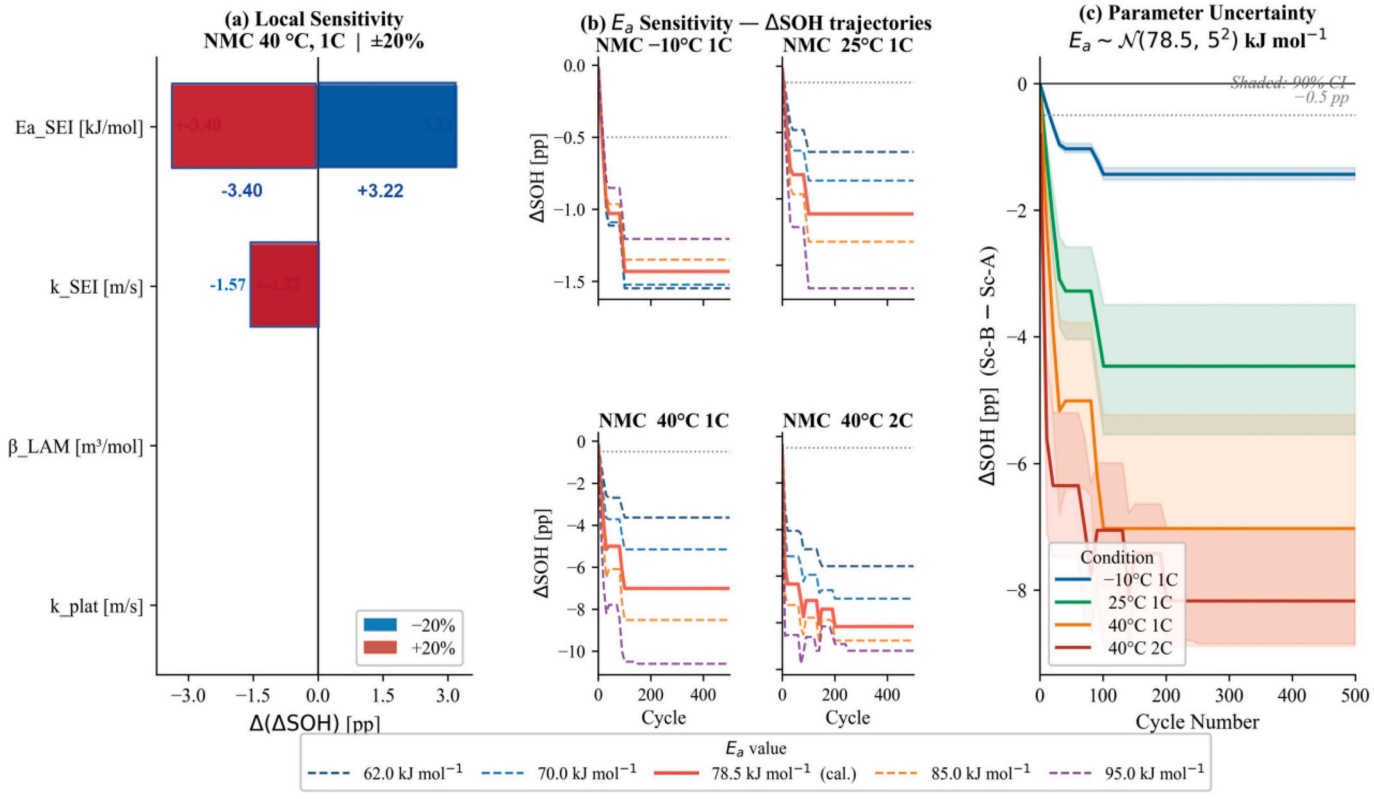

Fig. 6. Parameter uncertainty analysis for NMC cells under WLTP conditions. (a) Local sen-sitivity tornado chart at NMC 40 °C, 1C: ΔSOH change induced by 20% independent pertur-bation of each calibrated parameter. (b) E_a sensitivity: ΔSOH trajectories over 500 cycles for E_a 62, 70, 78.5, 85, 95 kJ mol^{-1} across all four representative Conditions. (C) Analytical Monte Carlo 90% credible interval: median ΔSOH (solid line) and 5th–95th percentile band (shaded) derived from $E_a \sim$ N (78.5, 5^2) kJ mol^{-1}.

− 3.40 pp. k_{SEI} contributes at the secondary level (±1.57 pp), reflecting its role in setting the absolute SEI rate from which both scenarios diverge equally; perturbations shift both Scenarios A and B but not their difference, except where the SEI trajectory becomes nonlinear. β_{LAM} and k_{plat} contribute <0.014 pp. and 0.000 pp. respectively, confirming that these parameters are essentially inert with respect to the isothermal ΔSOH error under WLTP conditions. This hierarchy is physically consistent: ΔSOH measures the *difference* in SEI rates between scenarios,

which is determined primarily by the Arrhenius temperature dependence (E_a) and secondarily by the absolute rate level (k_{SEI}), while mechanical and plating parameters affect both scenarios identically and therefore cancel in the difference.

4.5.2. E_a parametric sweep

Panel (b) shows the ΔSOH trajectories for all five E_a values across the four representative conditions. Three findings are noteworthy. First, at 25 °C/1C and 40 °C/1C, ΔSOH grows monotonically with E_a at all cycles, with no crossover. This confirms that the relationship between E_a and isothermal ΔSOH error is unambiguous and physically transparent. Second, even at the lowest published value of 62 kJ mol^{-1} [20], ΔSOH at cycle 500 reaches − 2.59 pp. at 25 °C and − 3.64 pp. at 40 °C/1C, both exceeding the 0.5 pp. significance threshold by a factor of five or more. The conclusion that the isothermal assumption is inadequate therefore holds across the entire physically plausible E_a range. Third, the − 10 °C condition shows minimal E_a sensitivity (range 0.34 pp. across all five values), because the Arrhenius factor at low temperature suppresses SEI growth so strongly that variations in E_a have limited impact on the absolute rate. This confirms the borderline status of the − 10 °C condition identified in Table 4.

4.5.3. Analytical Monte Carlo

Panel (c) shows the 90% credible interval bands for all four conditions, computed as described in Section 2.10. The 90% confidence intervals at cycle 500 are: NMC − 10 °C/1C: [− 1.52, −1.33] pp. (CI width 0.19 pp); NMC 25 °C/1C: [− 5.54, −3.49] pp. (CI width 2.05 pp); NMC 40 °C/1C: [− 8.89, −5.23] pp. (CI width 3.66 pp); NMC 40 °C/2C: [− 8.85, −7.02] pp. (CI width 1.83 pp). Critically, the 95th percentile bound representing the least conservative end of the uncertainty range remains at − 3.49 pp. at 25 °C and − 5.23 pp. at 40 °C/1C. Both values are well above the 0.5 pp. threshold by a margin of at least 4.7 pp. The conclusion that the isothermal ΔSOH error is practically significant is therefore robust to parameter uncertainty across the full calibration uncertainty space.

The detailed OAT sensitivity table for all four conditions is provided in Table S1 of the Supplementary Material.

4.6. Mechanism decomposition

Fig. 7 decomposes total capacity loss at cycle 500 into SEI, LAM, and plating contributions. Table 5 provides the numerical values.

For NMC, solid electrolyte interphase growth accounts for >99% of total capacity loss across all 12 NMC conditions, with loss of active material and plating each remaining below 0.015% of Q_{nom}. Notably, the absolute Q_{SEI} at 2C is lower than at 1C for both temperature conditions (4.20% vs 5.17% at 25 °C; 8.19% vs 10.99% at 40 °C): at the higher charge rate the cell reaches the upper voltage cutoff earlier, reducing delivered charge per cycle from 4.89 Ah to 4.74 Ah and therefore the cumulative SEI-active time integrated over 500 cycles. The shallow depth of discharge of 5.4% is insufficient to generate the mechanical stresses required for significant loss of active material, consistent with previous findings [8,24]. Solid electrolyte interphase dominance at shallow cycling is also confirmed experimentally [39].

For LFP at 1C (Table 6), the mechanism balance differs substantially. Solid electrolyte interphase contributes approximately 62% and loss of active material approximately 38% of total capacity loss. These percentages are fractions of total mechanism loss, not of Q_{nom}; the absolute values are 1.1–4.6% and 0.7–2.8% of Q_{nom} for solid electrolyte interphase and loss of active material respectively across the three LFP 1C

Table 5
ΔSOH at cycle 500 between isothermal and thermally coupled models. A negative value indicates the isothermal model underestimates degradation. † Below the 0.5 pp. threshold. ‡ LFP 2C excluded: solver instabilities.

Chemistry	T_{amb} [°C]	Rate	ΔSOH [pp]	Significant?
NMC	−10	1C	−1.43	Yes
NMC	−10	2C	−3.95	Yes
NMC	+25	1C	−4.46	Yes
NMC	+25	2C	−8.02	Yes
NMC	+40	1C	−7.03	Yes
NMC	+40	2C	−8.17	Yes
LFP	−10	1C	−0.40	No†
LFP	+25	1C	−0.50	Yes
LFP	+40	1C	−0.71	Yes
LFP	any	2C	excluded‡	

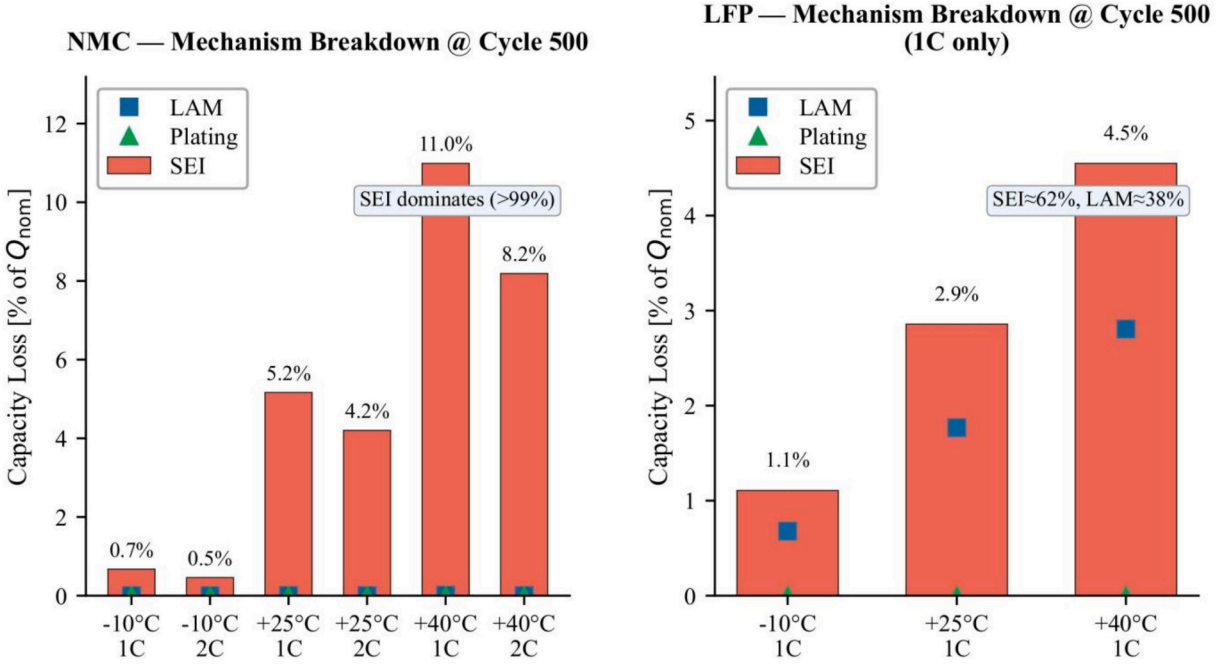

Fig. 7. Capacity loss mechanism breakdown at cycle 500. For NMC, solid electrolyte interphase (SEI) growth dominates (> 99%); for LFP at 1C, SEI contributes approximately 62% and loss of active material (LAM) approximately 38% of total capacity loss. LFP 2C conditions are excluded (Section 2.9).

Table 6
Mechanism resolved capacity loss at cycle 500 as % of $Q^{n}_{o,m}$. †Below 0.5 pp. significance threshold, chosen to exceed the typical SOH measurement uncertainty of 0.3–0.5 pp. reported for coulomb-counting methods in commercial BMS hardware. ‡LFP 2C conditions excluded, solver instabilities at the narrow voltage window produce non-physical trajectories (Section 2.9).

Chemistry	T_{amb} [°C]	Rate	Q_{SEI} [%]	Q^{LAM} [%]	Q_{plat} [%]
NMC	−10	1C	0.675	0.001	0.001
NMC	−10	2C	0.461	0.000	0.002
NMC	+25	1C	5.166	0.006	0.000
NMC	+25	2C	4.202	0.003	0.000
NMC	+40	1C	10.989	0.012	0.000
NMC	+40	2C	8.191	0.005	0.000
LFP	−10	1C	1.107	0.679	0.002
LFP	+25	1C	2.858	1.768	0.000
LFP	+40	1C	4.550	2.806	0.000
LFP	any	2C	excluded‡		

conditions. The elevated loss of active material fraction reflects LFP's larger depth of discharge per cycle (11.7%) and the larger calibrated β_{LAM} (coefficient).

Plating is negligible for all NMC conditions and for LFP at 1C. LFP 2C conditions are excluded from this analysis (Section 2.9).

Extreme case: NMC at −10 °C and 2C. Table 6 shows that for NMC at −10 °C/2C, $Q_{plat} = 0.002$ % of Q_{nom} at cycle 500 — the largest plating value among all NMC conditions yet still two orders of magnitude below $Q_{SEI} = 0.461$ %, confirming that plating remains negligible even under this combined cold-temperature and high-rate load. The ΔSOH at this condition is −3.95 pp. (Table 5), the third-largest NMC value overall, showing that the isothermal error is significant even when absolute capacity loss is small. The low absolute Q_{SEI} reflects Arrhenius suppression: at −10 °C the rate constant $k_{SEI}(T)$ is approximately 100× smaller than at 25 °C, so despite the large relative ΔSOH, total degradation is limited. Plating remains below the significance threshold because the WLTP 2C charge applied after a shallow 5.4 % DoD discharge does not drive the negative electrode overpotential sufficiently negative to sustain significant plating [1]. Sub-zero ambient temperatures combined with continuous fast charging above 3C from a deeply discharged state would be required for plating to become dominant conditions outside the WLTP protocol scope and a natural direction for future work.

4.7. Comparison with experimental reference data

Fig. 8 compares the calibrated model against the BatteryArchive NMC dataset at all three ambient temperatures.

To eliminate the charge-rate protocol mismatch, Scenarios A and B were re-run at 0.5C, the same charge rate as the BatteryArchive reference, and the resulting trajectories compared directly with the experimental data (Fig. 9). This constitutes a matched-protocol validation in which simulation and experiment share identical charge rate, cell chemistry, and ambient temperatures, directly addressing the protocol-mismatch concern raised for the main parametric sweep. The ΔSOH values at the matched rate are −0.52 pp. at −10 °C, −2.04 pp. at 25 °C, and −3.53 pp. at 40 °C, confirming that the isothermal ΔSOH error remains significant even at the reference charge rate. At 25 °C, the simulation brackets the BatteryArchive mean trajectory consistent with the calibration design (RMSE = 1.45 pp).

At −10 °C, both the calibrated model and the reference data show <3 pp. of fade over 500 cycles. The close agreement at this temperature is not coincidental: the Arrhenius factor at −10 °C suppresses SEI growth to approximately 1% of the 25 °C rate, making the absolute rate insensitive to the charge rate protocol mismatch. At 25 °C, the simulation at 1C charge (5.2 pp. loss at 500 cycles) brackets the reference trajectory from below, consistent with the higher charge rate. At 40 °C, the reference data shows substantial cell to cell variability and some specimens reach the 80% end of life threshold before cycle 500. The simulation underestimates this variability because the SPMe degradation model does not include cathode dissolution or electrolyte oxidation above 4.3 V, both of which become significant at high temperatures [41]. This constitutes a known limitation of the present model at elevated temperatures.

The BatteryArchive, CALCE, and NASA Ames reference datasets provide cycle-level capacity and SOH measurements but do not publish sub-cycle voltage or temperature time-series, precluding a direct simulated-versus- experimental comparison of these signals. The single-cycle electrochemical validation in Table [tab:validation] and the measured thermal rise of 13.4 °C (Section 3.1), which falls within the experimentally reported range for cylindrical cells of comparable size [56], provide the closest available validation of the model's voltage and temperature predictions given current data constraints.

The symmetric comparison between scenarios at all three tempera-

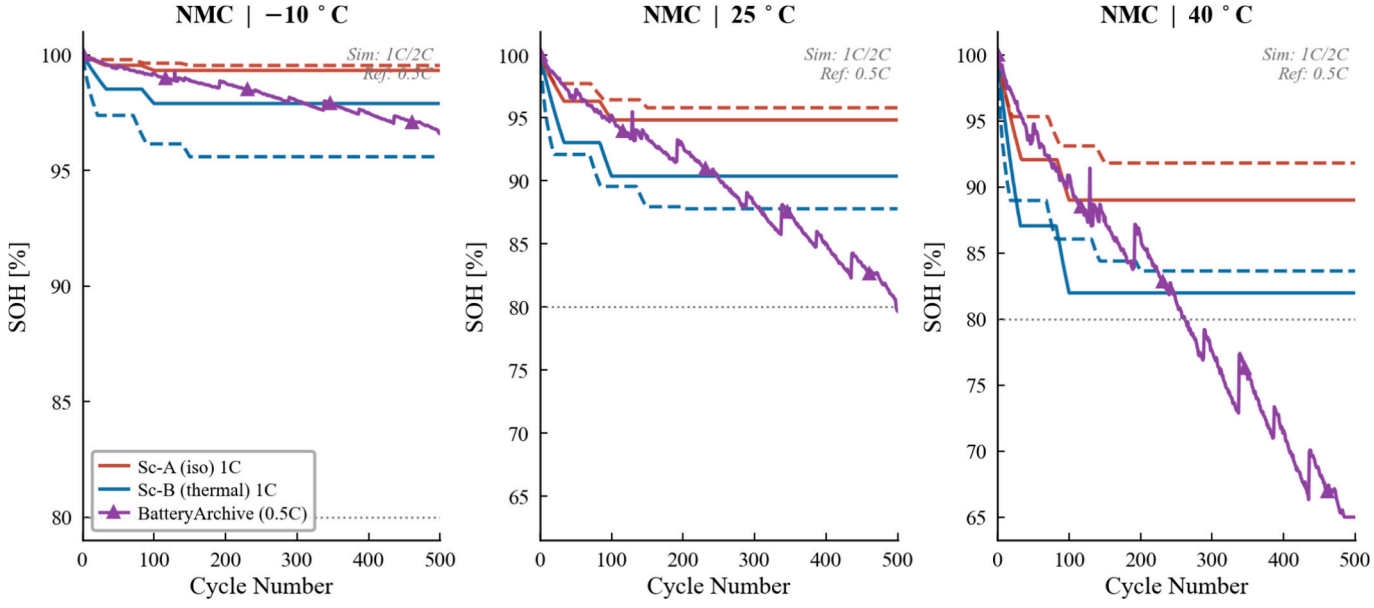

Fig. 8. Calibrated degradation model versus BatteryArchive NMC reference data at different temperatures. Isothermal and thermally coupled predictions are compared under varying charge rates.

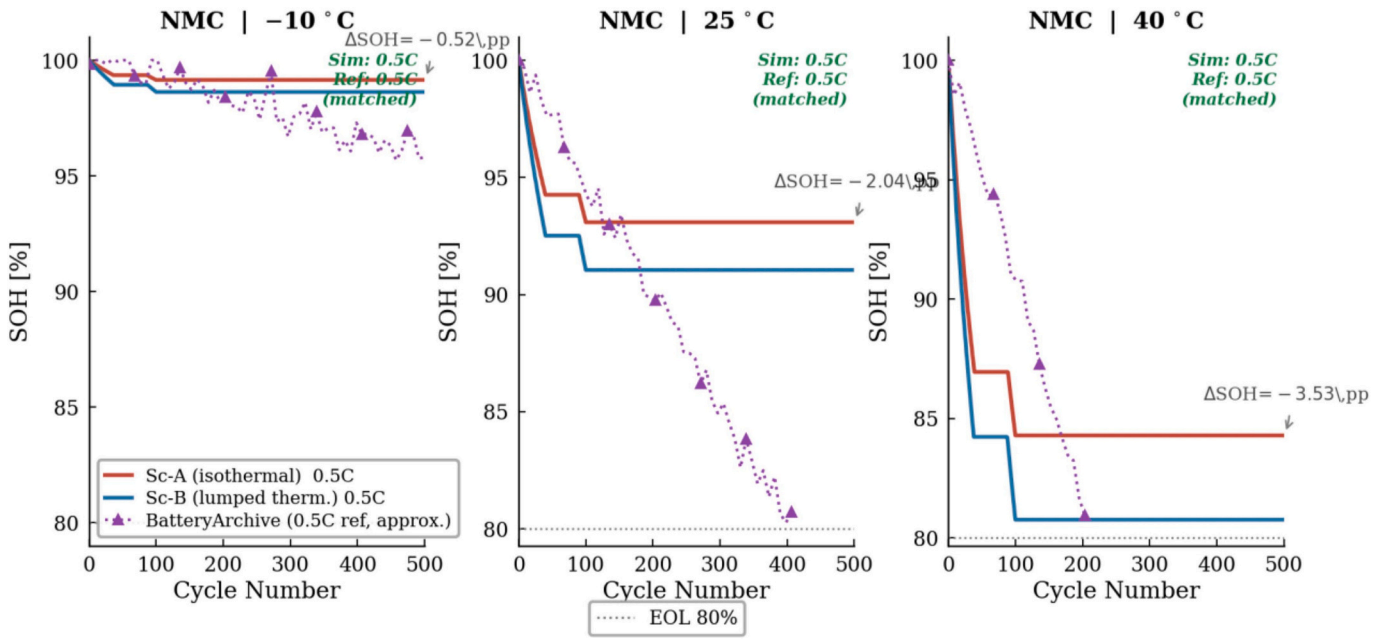

Fig. 9. Matched protocol validation: NMC simulations at 0.5C charge rate compared directly with the BatteryArchive reference at the same rate, eliminating the charge-rate mismatch. The ΔSOH between scenarios is − 0.52 pp. at − 10 °C, − 2.04 pp. at 25 °C, and − 3.53 pp. at 40 °C.

tures confirms the unidirectional nature of the isothermal ΔSOH error: Scenario B always predicts lower SOH than Scenario A when $E_a > 0$, and the gap is largest at the highest temperature and charge rate where self heating is greatest. This symmetry validates the physical mechanism proposed in Section 4.4 and is consistent with the Arrhenius amplification analysis in Fig. 3.

4.8. Implications for battery management system design

The results have direct practical implications for BMS algorithm designers choosing between isothermal and thermally coupled degradation models. The following decision rule is supported by the parametric sweep: a lumped thermal model becomes increasingly justified when the SEI activation energy of the cell chemistry exceeds approximately 40 kJ mol^{-1}. This threshold is obtained by extrapolating the calibrated Arrhenius–ΔSOH relationship below the parametric sweep range of 62–95 kJ mol^{-1} and carries unquantified extrapolation uncertainty; it should be treated as an order-of-magnitude indicator rather than a precise design boundary. Below this threshold, the Arrhenius amplification of the 3.8–6.7 K (NMC, 1C) WLTP thermal gradient reported in Section 4.1 is insufficient to produce 0.5 pp. over 500 cycles.

The computational overhead of the lumped thermal model is minimal: the single node energy balance adds one state variable and requires only cell mass, heat capacity, and convective coefficient as additional parameters, all of which are measurable from standard calorimetry. In contrast to spatially resolved thermal models that require internal temperature sensors [56], the lumped model is compatible with standard BMS hardware that measures only the surface temperature. To contextualise the sweep runtime of 1.15 h for 24 conditions at 500 cycles each: equivalent DFN simulations would require approximately 10^2–10^3 times longer per cycle owing to the full spatial resolution of concentration and potential fields [40], making a 24-condition sweep computationally prohibitive without high-performance computing resources. The SPMe therefore provides the only practically tractable framework for the multi-condition parametric study reported here.

Although only 1C and 2C were simulated, the underlying physical mechanism, Arrhenius amplification of self-heating predicts a monotonic trend at other rates. Below 1C, heat generation scales with I^2 (Eq. 5), so ΔSOH is expected to be smaller than the 1C values reported here. Above 2C, ΔSOH is expected to exceed the 2C values, consistent with the monotone 1C→2C trend already observed (Table 5). This extrapolation is physically motivated but not directly simulated outside $\{1, 2\}$(C).

The single-node energy balance (Eq. 4) adds one scalar state and negligible memory overhead, and is compatible with microcontroller-class BMS hardware operating at cycle-level update intervals, where the thermal state changes slowly relative to the electrochemical dynamics. Typical automotive BMS microcontrollers (e.g. Renesas RH850, NXP S32K series) provide 64–256 kB of RAM at 32-bit precision; the single thermal state and its Euler update require fewer than 50 floating-point operations and under 100 bytes of additional memory per cycle step, well within the resource envelope of embedded hardware certified to ISO 26262. Real-time integration at cycle-level resolution is therefore feasible without dedicated co-processor support.

Long-term ΔSOH behaviour beyond 500 cycles: SEI growth follows a diffusion-limited $\sqrt{t}$ (equivalently $\sqrt{n}$) regime, so the instantaneous growth rate per cycle decreases monotonically with cycle number. However, Scenario B permanently operates at a higher temperature than Scenario A because self-heating is sustained by ongoing cycling throughout the battery lifetime. The Arrhenius amplification of the SEI rate in Scenario B relative to Scenario A is therefore never zero, and the ΔSOH gap continues to widen beyond cycle 500 but at a *decelerating rate* proportional to $\sqrt{n}$. Extrapolating the calibrated $\sqrt{n}$ scaling, the NMC 25 °C/1C gap of 4.46 pp. at cycle 500 is expected to reach approximately $4.46 \times \sqrt{1000/500} \approx 6.3$ pp. by cycle 1000, and $4.46 \times \sqrt{2000/500} \approx 8.9$ pp. by cycle 2000. The gap does not saturate or reverse, because the permanent Arrhenius offset between scenarios is maintained as long as heat generation continues. This long-term divergence further reinforces the case for including a lumped thermal model in BMS degradation estimators, particularly for fleet assets operated over multi-year service lives where the accumulated SOH prediction bias would substantially exceed the 500-cycle values reported here.

It is important to scope these conclusions appropriately. The comparison throughout this study is strictly between an isothermal model (Scenario A) and a lumped single-node thermal model (Scenario B); spatially resolved thermal models are not evaluated. The lumped model captures the average temperature rise of the cell but cannot represent internal temperature gradients. For prismatic or large-format pouch cells, where internal gradients can exceed 5 °C under fast charging [50],

a spatially resolved thermal model coupled to the electrochemistry may be necessary even under WLTP-like loading. Beyond the lumped model, two further levels of thermal fidelity are relevant for future work: a DFN–thermal coupled model that resolves electrode-scale heat generation and radial temperature gradients within the cell, and a pack-level thermal model that accounts for cell-to-cell temperature non-uniformity driven by coolant flow and pack geometry. The present results and decision rule therefore apply specifically to cylindrical cells under drive-cycle duty conditions with charge rates up to 2C, and should not be extrapolated to continuous high-rate charging scenarios above 3C or to large-format cells with poor thermal conductivity. Furthermore, the calibration is specific to graphite-based anodes paired with NMC and LFP cathodes; other cathode chemistries such as NCA, LMFP, or LMO, and silicon-blended anodes with higher activation energies and mechanically driven LAM, are outside the validated scope and may exhibit different isothermal ΔSOH error magnitudes. Extension of the two-stage calibration procedure to these chemistries constitutes a natural direction for future work. The present model uses a liquid electrolyte formulation; alternative systems including polymer and solid-state electrolytes [61] introduce fundamentally different interfacial chemistry and degradation pathways that are outside the scope of the current framework but represent a compelling direction for future extension.

5. Conclusion

This study developed and calibrated a multi-mechanism electrochemical-thermal degradation model to quantify the SOH prediction error introduced by the isothermal assumption under WLTP drive cycles. Four findings emerge.

The isothermal assumption introduces a practically significant SOH error whenever Ea is physically realistic. With the calibrated $Ea = 78.5$ kJ mol^{-1}, the error ranges from 1.4 to 8.2 percentage points (pp) over 500 cycles (NMC), compared with a maximum of 0.20 pp. at $Ea = 0$. This error is governed by the SEI activation energy rather than the drive-cycle thermal gradient. The two-stage calibration procedure used to determine Ea avoids the degenerate minimum encountered in single-parameter kSEI optimization and achieves an RMSE of 1.45 pp. against BatteryArchive NMC data, representing a 6.3-fold improvement over the uncalibrated default. SEI growth dominates NMC capacity loss (>99%), whereas for LFP, SEI and LAM contribute approximately 62% and 38%, respectively, reflecting the larger depth of discharge. Lithium plating remains negligible under WLTP loading in all reported conditions.

A three-layer uncertainty analysis confirms the robustness of these findings. The activation energy (Ea) is the dominant source of SOH difference (ΔSOH) variation, whereas βLAM and $k$plat have negligible influence. Even at the lowest published Ea (62 kJ mol^{-1}), ΔSOH exceeds 2.5 pp. at 25 °C, and the 90% Monte Carlo credible interval remains well above the 0.5 pp. significance threshold across all tested conditions. Practically, a lumped thermal model becomes increasingly justified when Ea exceeds approximately 40 kJ mol^{-1} (an extrapolated, order-of-magnitude indicator), reducing NMC SOH prediction error by 1.4–8.2 pp. per 500 cycles for cylindrical cells under drive-cycle duty up to 2C, while incurring negligible computational overhead. Future work should extend the calibration procedure to additional battery chemistries, fast-charging conditions, and large-format cell geometries beyond the scope of the present study.

CRediT authorship contribution statement

Nadim Ahmed: Writing – review & editing, Writing – original draft, Software, Methodology, Data curation, Conceptualization. **Md Fazle Hasan Shiblee:** Writing – review & editing, Writing – original draft, Visualization, Software, Investigation. **Theodore Azemtsop Manfo:** Writing – review & editing, Writing – original draft, Validation, Supervision, Project administration, Methodology, Investigation, Formal analysis.

Declaration of generative AI and AI-assisted technologies in the writing process

During the preparation of this work the authors used ChatGPT and Grammarly to improve language clarity. After using these tools, the authors reviewed and edited the content as needed and take full responsibility for the content of the publication.

Funding

This research did not receive any specific grant from funding agencies in the public, commercial, or not-for-profit sectors.

Declaration of competing interest

The authors declare that they have no known competing financial interests or personal relationships that could have appeared to influence the work reported in this paper.

Appendix A. Supplementary data

Supplementary data to this article can be found online at https://doi.org/10.1016/j.apenergy.2026.128623.

Data availability

Data will be made available on request.

References

[1] Edge JS, O'Kane S, Prosser R, Kirkaldy ND, Patel AN, Hales A, et al. Lithium ion battery degradation: what you need to know. Phys Chem Chem Phys 2021;23(14):8200–21. https://doi.org/10.1039/D1CP00359C.
[2] Ng M-F, Zhao J, Yan Q, Conduit GJ, Seh ZW. Predicting the state of charge and health of batteries using data-driven machine learning, nature. Machine Intelligence 2020;2:161–70. https://doi.org/10.1038/s42256-020-0156-7.
[3] Zhang R, Xia B, Li B, Cao L, Lai Y, Zheng W, et al. State of the art of lithium-ion battery SOC estimation for electrical vehicles. Energies 2018;11(7):1820. https://doi.org/10.3390/en11071820.
[4] Che Y, Deng Z, Lin X, Hu X, Bae C, Yin Y. Predictive battery health management with transfer learning and online model correction. IEEE Trans Veh Technol 2021;70(2):1269–77. https://doi.org/10.1109/TVT.2021.3055811.
[5] Merla Y, Wu B, Yufit V, Martinez-Botas RF, Offer GJ. An easy-to-parameterise physics-informed battery model and its application towards lithium-ion battery cell design, diagnosis, and degradation. J Power Sources 2021;484:229295. https://doi.org/10.1016/j.jpowsour.2020.229295.
[6] Sebbagh T, Manfo TA, Şahin ME. Advances in battery technologies for next-generation energy storage systems. Electronics 2026;15(3):690. https://doi.org/10.3390/electronics15030690.
[7] Paulson NH, Kubal J, Ward L, Saxena S, Lu W, Babinec SJ. Feature engineering for machine learning enabled early prediction of battery lifetime. J Power Sources 2022;527:231127. https://doi.org/10.1016/j.jpowsour.2022.231127.
[8] Reniers JM, Mulder G, Howey DA. Review and performance comparison of mechanical-chemical degradation models for lithium-ion batteries. J Electrochem Soc 2019;166(14):A3189–200. https://doi.org/10.1149/2.0281914jes.
[9] Doyle M, Fuller TF, Newman J. Modeling of galvanostatic charge and discharge of the lithium/polymer/insertion cell. J Electrochem Soc 1993;140(6):1526–33. https://doi.org/10.1149/1.2221597.
[10] Planella FB, Ai W, Boyce AM, Ghosh A, Korotkin I, Sahu S, et al. A continuum of physics-based lithium-ion battery models reviewed. Progress in Energy 2022;4(4):042003. https://doi.org/10.1088/2516-1083/ac7d31.
[11] Marquis SG, Sulzer V, Timms R, Please CP, Chapman SJ. An asymptotic derivation of a single particle model with electrolyte. J Electrochem Soc 2019;166(15):A3693–706. https://doi.org/10.1149/2.0341915jes.
[12] Timms R, Marquis SG, Sulzer V, Please CP, Chapman SJ. Asymptotic reduction of a lithium-ion pouch cell model. SIAM Journal on Applied Mathematics 2021;81(3):765–88. https://doi.org/10.1137/20M1336898.
[13] Richardson G, Korotkin I. Generalised single particle models for high-rate operation of graded lithium-ion electrodes: systematic derivation and validation. Electrochim Acta 2020;339:135862. https://doi.org/10.1016/j.electacta.2020.135862.
[14] Kosch S, Zhao Y, Sturm J, Schuster J, Mulder G, Ayerbe E, et al. A computationally efficient multi-scale model for lithium-ion cells. J Electrochem Soc 2018;165(10):A2374–88. https://doi.org/10.1149/2.0011811jes.

[15] Hales A, Diaz LB, Marzook MW, Patel Y, Jeong Y, Offer G. The cell cooling coefficient: a standard to define heat rejection from lithium-ion batteries. J Electrochem Soc 2019;166(12):A2383–95. https://doi.org/10.1149/2.0191912jes.
[16] Kim J, Oh J, Lee H. Review on battery thermal management system for electric vehicles. Appl Therm Eng 2019;149:192–212. https://doi.org/10.1016/j.applthermaleng.2018.12.020.
[17] Das S, Bhatt D, Offer GJ, Patel Y. Electrolyte mediated suppression of the solid-electrolyte interphase on graphite anodes: an electrochemical and surface study. Electrochim Acta 2019;318:416–25. https://doi.org/10.1016/j.electacta.2019.06.044.
[18] Manfo TA. A comprehensive analysis of material revolution to evolution in lithium-ion battery technology. Turkish Journal of Materials 2023;8(1):1–3.
[19] Theodore AM. Promising cathode materials for rechargeable lithium-ion batteries: a review, journal of sustainable. Energy 2023;14:51–8.
[20] Schimpe M, von Kuepach ME, Naumann M, Hesse HC, Smith K, Jossen A. Comprehensive modeling of temperature-dependent degradation mechanisms in lithium iron phosphate batteries. J Electrochem Soc 2018;165(2):A181–93. https://doi.org/10.1149/2.1181714jes.
[21] Peled E, Menkin S. Review: SEI: past, present and future. J Electrochem Soc 2017;164(7):A1703–19. https://doi.org/10.1149/2.1441707jes.
[22] Naumann M, Schimpe M, Keil P, Hesse HC, Jossen A. Analysis and modeling of calendar aging of a commercial LiFePO4/graphite cell. J Energy Storage 2018;17:153–69. https://doi.org/10.1016/j.est.2018.01.019.
[23] Zhao Y, Stein P, Bai Y, Al-Siraj M, Yang Y, Xu B-X. A review on modeling of electro-chemo-mechanics in lithium-ion batteries. J Power Sources 2019;413:259–83. https://doi.org/10.1016/j.jpowsour.2018.12.011.
[24] Ai W, Kraft L, Sturm J, Jossen A, Wu B. Electrochemical thermal-mechanical modelling of stress inhomogeneity in lithium-ion pouch cells. J Electrochem Soc 2020;167(1):013512. https://doi.org/10.1149/2.0122001JES.
[25] Ecker M, Nieto N, Käbitz S, Schmalstieg J, Blanke H, Warnecke A, et al. Calendar and cycle life study of Li(NiMnCo)O2-based 18650 lithium-ion batteries. J Power Sources 2014;248:839–51. https://doi.org/10.1016/j.jpowsour.2013.09.143.
[26] Theodore AM. Structural, electrical, and electrochemical studies of the olivine LiMPO4 (M=Fe, Co, Cr, Mn, V) as cathode materials for lithium-ion rechargeable batteries based on the intercalation principle. Materials Open Research 2023;2:11. https://doi.org/10.12688/materialsopenres.17543.1.
[27] Manfo TA, Laaksonen H. A comparative study of the modified high voltage olivine-phosphate LiMPO4 (M=Fe, Mn, Co, Ni) as promising cathode materials for next-generation rechargeable batteries. J Energy Storage 2026;160:121797. https://doi.org/10.1016/j.est.2026.121797.
[28] O'Kane SEJ, Campbell ID, Marzook MWJ, Offer GJ, Marinescu M. Physical origin of the differential voltage minimum associated with lithium plating in Li-ion batteries. J Electrochem Soc 2020;167(9):090540. https://doi.org/10.1149/1945-7111/ab90ac.
[29] Waldmann T, Iturrondobeitia A, Kasper M, Ghanbari N, Aguesse F, Bekaert E, et al. Review: post-mortem analysis of aged lithium-ion batteries: disassembly methodology and physico-chemical analysis techniques. J Electrochem Soc 2016;163(10):A2149–64. https://doi.org/10.1149/2.1211610jes.
[30] Dose WM, Temprano I, Allen JP, Bjorklund E, O'Keefe CA, Li W, et al. Electrolyte reactivity at the charged Ni-rich cathode interface and degradation in Li-ion batteries. ACS Energy Letters 2022;7(10):3524–34. https://doi.org/10.1021/acsenergylett.2c01818.
[31] Theodore AM, Adam AA, Dhapola PS. Effect of layered, spinel, and olivine-based positive electrode materials on rechargeable lithium-ion batteries: a review. Journal of Computational Mechanics 2023;6(4).
[32] Plett GL. Battery management systems, volume I: battery modeling. Norwood, MA: Artech House; 2015.
[33] Chen C-H, Planella FB, O'Regan K, Gastol D, Widanage WD, Kendrick E. Development of experimental techniques for parameterization of multi-scale lithium-ion battery models. J Electrochem Soc 2020;167(8):080534. https://doi.org/10.1149/1945-7111/ab9050.
[34] United Nations economic Commission for Europe, global technical regulation no. 15: Worldwide harmonised light vehicles test procedure, Tech. Rep. ECE/TRANS/180/Add.15, UNECE (2014). URL, https://unece.org/transport/standards/transport/vehicle-regulations-wp29/global-technical-regulations.
[35] Tosi L, Hales A, Rummens H, Bhatt D, Offer GJ, Patel Y. Degradation of lithium-ion battery under real driving cycles. J Electrochem Soc 2020;167(9):090557. https://doi.org/10.1149/1945-7111/ab9c82.
[36] Dubarry M, Baure G, Devie A. Durability and reliability of EV batteries under electric utility grid operations: PATH dependence of battery degradation. J Electrochem Soc 2018;165(5):A773–83. https://doi.org/10.1149/2.0421805jes.
[37] Safari M, Morcrette M, Teyssot A, Delacourt C. Multimodal physics-based aging model for life prediction of Li-ion batteries. J Electrochem Soc 2009;156(3):A145–53. https://doi.org/10.1149/1.3043429.
[38] Prada E, Di Domenico D, Creff Y, Bernard J, Sauvant-Moynot V, Huet F. A simplified electrochemical and thermal aging model of LiFePO4-graphite Li-ion batteries: power and capacity fade simulations. J Electrochem Soc 2013;160(4):A616–28. https://doi.org/10.1149/2.053304jes.
[39] Kabitz S, Gerschler JB, Ecker M, Yurdagel Y, Emmermacher B, André D, et al. Cycle and calendar life study of a graphite LiNi1/3Mn1/3Co1/3O2 Li-ion high energy system. Part a: full-cell characterization. J Power Sources 2013;239:572–83. https://doi.org/10.1016/j.jpowsour.2013.03.045.
[40] Sulzer V, Marquis SG, Timms R, Robinson M, Chapman SJ. PyBaMM: fast and flexible simulations of battery models in Python. J Electrochem Soc 2021;168(8):080534. https://doi.org/10.1149/1945-7111/ac085f.
[41] Rinkel BLD, Hall DS, Temprano I, Grey CP. Electrolyte oxidation pathways in lithium-ion batteries. J Am Chem Soc 2020;142(35):15058–74. https://doi.org/10.1021/jacs.0c06363.
[42] Attia PM, Grover A, Jin N, Severson KA, Markov TM, Liao Y-H, et al. Closed-loop optimization of fast-charging protocols for batteries with machine learning. Nature 2020;578:397–402. https://doi.org/10.1038/s41586-020-1994-5.
[43] Severson KA, Attia PM, Jin N, Perkins N, Jiang B, Yang Z, et al. Data-driven prediction of battery cycle life before capacity degradation, nature. Energy 2019;4:383–91. https://doi.org/10.1038/s41560-019-0356-8.
[44] Jeon DH, Kim S, Hempelmann R. State-of-the-art review of degradation mechanisms of commercial lithium-ion batteries. J Power Sources 2025;646:237242. https://doi.org/10.1016/j.jpowsour.2025.237242.
[45] Li R, Kirkaldy ND, Oehler FF, Marinescu M, Offer GJ, O'Kane SEJ. The importance of degradation mode analysis in parameterising lifetime prediction models of lithium-ion battery degradation. Nat Commun 2025;16:2776. https://doi.org/10.1038/s41467-025-57968-3.
[46] Zhang H, Altaf F, Wik T. Synthetic dataset of LG M50 batteries with different degradation pathways. Data Brief 2024;57:111076. https://doi.org/10.1016/j.dib.2024.111076.
[47] Wheeler W, Bultel Y, Venet P, Sari A. Degradation of a lithium-ion battery cell for enhanced first and second life: effects of temperature, orientation, C-rate and state of charge. Batteries 2026;12(4):121. https://doi.org/10.3390/batteries12040121.
[48] Naguib M, Chen J, Kollmeyer P, Emadi A. Thermal fault detection of lithium-ion battery packs through an integrated physics and deep neural network based model. Communications Engineering 2025;4:79. https://doi.org/10.1038/s44172-025-00409-2.
[49] Mattia L, Beiranvand H, Zamboni W, Liserre M. Lithium-ion battery thermal modelling and characterisation: a comprehensive review. J Energy Storage 2025. https://doi.org/10.1016/j.est.2025.018274.
[50] Mannapperuma V, Gaddala LC, Zheng R, Kim D, Kim Y, Ullal A, et al. Electro-thermal modeling and parameter identification of an EV battery pack using drive cycle data. Batteries 2025;11(9):319. https://doi.org/10.3390/batteries11090319.
[51] Bernardi D, Pawlikowski E, Newman J. A general energy balance for battery systems. J Electrochem Soc 1985;132(1):5–12. https://doi.org/10.1149/1.2113792.
[52] He W, Williard N, Chen C, Pecht M. State of health estimation for Li-ion batteries using incremental capacity analysis, in. IEEE Conference on Prognostics and Health Management 2011;2011:1–6. https://doi.org/10.1109/ICPHM.2011.6024342.
[53] Saha B, Goebel K. Battery data set, NASA Ames Prognostics Data Repository. https://ti.arc.nasa.gov/tech/dash/groups/pcoe/prognostic-data-repository/; 2007.
[54] Saltelli A, Tarantola S, Campolongo F, Ratto M. Sensitivity analysis in practice: a guide to assessing scientific models. Chichester, UK: John Wiley & Sons; 2004.
[55] Prada E, Di Domenico D, Creff Y, Bernard J, Sauvant-Moynot V, Huet F. Simplified electrochemical and thermal model of LiFePO4-graphite Li-ion batteries for fast charge applications. J Electrochem Soc 2012;159(9):A1508–19. https://doi.org/10.1149/2.064209jes.
[56] Lin X, Perez HE, Siegel JB, Stefanopoulou AG, Li Y, Anderson RD, et al. Online parameterization of lumped thermal dynamics in cylindrical lithium ion batteries for core temperature estimation and health monitoring. IEEE Trans Control Syst Technol 2013;21(5):1745–55. https://doi.org/10.1109/TCST.2012.2217143.
[57] Chaudhari T, Chakravorty S. Analysis and advancements of the state of charge estimation methods in smart battery management system supported by lithium-ion battery operated electric vehicles. Next Energy 2025;8:100337. https://doi.org/10.1016/j.nxener.2025.100337.
[58] The state of health estimation of lithium-ion batteries. A review of health indicators, estimation methods, development trends and challenges. World Electr Veh J 2025;16(8):429. https://doi.org/10.3390/wevj16080429.
[59] Pang MC, Yang K, Brugge R, Zhang T, Liu X, Pan F, et al. Interactions are important: linking multi-physics mechanisms to the performance and degradation of solid-state batteries. Materials Today Physics 2021;21:100519. https://doi.org/10.1016/j.mtphys.2021.100519.
[60] Xu B, Oudalov A, Ulbig A, Andersson G, Kirschen DS. Modeling of lithium-ion battery degradation for cell life assessment. IEEE Transactions on Smart Grid 2018;9(2):1131–40. https://doi.org/10.1109/TSG.2016.2578950.
[61] Badi N, Theodore AM, Alghamdi SA, Al-Aoh HA, Lakhouit A, Singh PK, et al. The impact of polymer electrolyte properties on lithium-ion batteries. Polymers 2022;14:3101. https://doi.org/10.3390/polym14153101.